

1 **An improved method of Newmark analysis for mapping hazards of**  
2 **co-seismic landslides**

3

4 **Mingdong Zang<sup>a,b,c</sup>, Shengwen Qi<sup>a,b,c,\*</sup>, Yu Zou<sup>a,b,c</sup>, Zhuping Sheng<sup>d</sup>, Blanca S. Zamora<sup>d</sup>**

5

6 *<sup>a</sup> Key Laboratory of Shale Gas and Geoengineering, Institute of Geology and Geophysics, Chinese*  
7 *Academy of Sciences, Beijing 100029, China*

8 *<sup>b</sup> Institutions of Earth Science, Chinese Academy of Sciences, Beijing 100029, China*

9 *<sup>c</sup> University of Chinese Academy of Sciences, Beijing 100029, China*

10 *<sup>d</sup> Texas A&M AgriLife Research Center at El Paso, El Paso, Texas 79927, USA*

11

12 \* Corresponding Author.

13 *E-mail address: [qishengwen@mail.iggcas.ac.cn](mailto:qishengwen@mail.iggcas.ac.cn) (S. W. Qi)*

14

15

16 **Abstract**

17 Coseismic landslides have been responsible for destroyed buildings and structures, dislocated roads  
18 and bridges, cut off of pipelines and lifelines, and tens of thousands of deaths. Accurately mapping the  
19 hazards of coseismic landslides is an important and ~~challenge~~ work. Newmark's method is widely applied  
20 to assess the permanent displacement along a potential slide surface to determine the coseismic responses  
21 of the slope. This paper considers the roughness and size effect of the potential slide surface-unloading  
22 joint, and then presents an improved method of Newmark analysis for mapping hazard of coseismic  
23 landslides. The improved method is verified using data from a case study of the 2014  $M_w$  6.1 (USGS)  
24 Ludian earthquake in Yunnan Province, China. The permanent displacement yielded from this method  
25 range from 0 to 122 cm. Comparisons are made between the predicted displacements and a comprehensive  
26 inventory of landslides triggered by the Ludian earthquake to map the spatial variability using certainty  
27 factor model (CFM). Confidence levels of coseismic landslides indicated by certainty factors range from  
28 -1 to 0.95. A coseismic landslide hazard map is then produced based on the spatial distribution of the  
29 values of certainty factors. Area under the curve analysis is used to draw a comparison between the  
30 improved and conventional method of Newmark analysis, revealing the improved performance of the  
31 method presented in this paper. Such method can be applied to predict the hazard zone of the region and  
32 provide guidelines for making decisions regarding infrastructure development and post-earthquake  
33 reconstruction.

34

35 *Keywords:* Coseismic landslide; Newmark's method; Barton model; Certainty factor; Hazard Mapping

36 **1. Introduction**

37 One of the major causes of landslides is recognized as the earthquake. Coseismic landslide hazards  
38 have drawn increasing attention in recent years (i.e. [Jibson et al., 1998, 2000](#); [Khazai and Sitar, 2004](#); [Qi  
39 et al., 2010, 2011, 2012](#); [Chen et al., 2012](#); [Xu et al., 2013](#); [Yuan et al., 2014](#)). In fact, the damage caused  
40 by seismically triggered landslides is sometimes more severe than the damage direct from the earthquake  
41 ([Keefer, 1984](#)). Estimating where is likely to have slope failure under a specific shaking condition plays  
42 an important role in regional assessment of coseismic landslides.

43 Pseudostatic analysis formalized by [Terzaghi \(1950\)](#) and finite-element modeling applied by [Clough  
44 and Chopra \(1966\)](#) were employed to assess the seismic stability of slopes in early efforts ([Jibson, 2011](#)).  
45 [Newmark \(1965\)](#) first introduced a relatively simple and practical method, still commonly used, to  
46 estimate the coseismic permanent-displacements of slopes ([Jibson, 2011](#)). Studies showed that  
47 Newmark's method yields reasonable and practical results when modeling the dynamic performance of  
48 natural slopes ([Wilson and Keefer, 1983](#); [Wieczorek et al., 1985](#); [Jibson et al., 1998, 2000](#); [Pradel et al.,  
49 2005](#)). Recent years, [Rathje and Antonakos \(2011\)](#) present a unified framework for predicting coseismic  
50 permanent sliding displacement based on Newmark's method. [Chen et al. \(2018\)](#) used Newmark's method  
51 to calculate the minimum accelerations required for coseismic landslides in the affected region of 2014  
52 Ludian earthquake. [Chen et al. \(2019\)](#) subsequently developed an easy-operation mapping method to  
53 assess coseismic landslide hazard in the quake zone of 2014 Ludian earthquake, with the help of  
54 Newmark's method.

55 Such applications generally start from an analysis of the dynamic stability of slopes that is quantified  
56 as the critical acceleration. Barton model ([Barton, 1973](#)) has been widely used in rock mechanics and

57 engineering field to predict the shear strength of rock joints, which plays a crucial role in the calculation  
58 of critical acceleration. However, researches do not pay enough attentions on the shear strength of rock  
59 joints during the assessment of coseismic landslides. To better estimate the dynamic stability of slopes, in  
60 this paper, we introduce the Barton model (Barton, 1973) into a Newmark analysis to develop an improved  
61 modeling method for mapping hazards of coseismic landslides, using data from the 2014 Ludian  
62 earthquake in Yunnan Province, Southwestern China. As predictions of coseismic landslides are not only  
63 based on exact results, i.e., computed permanent-displacements, but also mingled with unformalized  
64 expertise (Shortliffe and Buchanan, 1975), i.e., interpreted landslides, we then present a model of inexact  
65 reasoning method, which defies analysis as applications of sets of inference rules that are expressed in  
66 the predicate logic (Shortliffe and Buchanan, 1975), to produce a coseismic landslide hazard map.

67 This paper briefly introduces the site characteristics and the spatial distribution of triggered  
68 landslides, describes the modeling method used for the analysis of seismic slope stability, then presents  
69 the mapping procedure of the confidence level of seismic slope-failure, and finally discusses the results  
70 of the seismic hazard assessment and the comparison with a conventional Newmark analysis.

71

## 72 **2. Study area**

73 The epicenter of the 2014  $M_w$  6.1 Ludian earthquake is located in the southeastern margin of the  
74 Tibetan plateau. A rectangular area lying immediately around the epicenter and containing dense  
75 concentrations of induced landslides was chosen for study. Elevation in the study area ranges from 785  
76 m to 3,085 m above the sea. There are three rivers, the Niulanjiang River, the Shaba River and the  
77 Longquan River passing through the area. The topography ranges from flat in river valleys to nearly

78 vertical in the slopes on the side of the rivers. The Niulanjiang River, flowing from southeast (SE) to the  
79 northwest (NW), where according to Chen et al. (2015), incises down to a depth between 1,200 m and  
80 3,300 m, resulting in about 80% of the slopes with angles greater than 40° distributed along the banks.  
81 Predominant geologic units of the study area vary ~~in the era~~ from Proterozoic to Mesozoic, including  
82 dolomite, limestone, shale, sandstone, basalt and slate.

83 A landslide inventory containing 1,416 landslides (Fig. 1) was posed by visual interpretation through  
84 comparison between pre-earthquake satellite images from Google Earth (January 30, 2014) and 0.2m-  
85 high-resolution post-earthquake aerial images (August 7, 2014, data provided by Digital Mountain and  
86 Remote Sensing Applications Center, Institute of Mountain Hazards and Environment, Chinese Academy  
87 of Sciences; Beijing Anxiang Power Technology Co., LTD.). A majority of landslides triggered in this  
88 earthquake were shallow flow-like landslides (less than 3 m deep) developing in particularly dense  
89 concentrations along steeply incised river valleys. The total area of these interpreted landslides was 7.01  
90 km<sup>2</sup> within a study area of 705 km<sup>2</sup>. A detailed study showed that 846 of the mapped landslides were  
91 greater than 1,000 m<sup>2</sup>, occupying 6.74 km<sup>2</sup> and accounting for 96.1% of the total landslide area, out of  
92 which 279 of the mapped landslides were greater than 5,000 m<sup>2</sup>, occupying 5.37 km<sup>2</sup> and accounting for  
93 76.6% of the total landslide area.

94

### 95 **3. Methodology**

#### 96 3.1 Modeling method

97 In the context of the analysis of the dynamic stability of a slope, Newmark (1965) proposed a  
98 permanent-displacement analysis that bridges the gap between simplistic pseudostatic analysis and

99 sophisticated, but generally impractical finite-element modeling (Jibson, 1993). Newmark's method  
100 simulates a landslide as a rigid-plastic friction block having a known critical acceleration on an inclined  
101 plane (Fig. 2), and then calculates the cumulative permanent displacement of the block as it is subjected  
102 to an acceleration-time history of an earthquake. Newmark (1965) showed that the dynamic stability of a  
103 slope is related to the critical acceleration of a potential landslide block, and it can be expressed as a  
104 simple function of the static factor of safety and the landslide geometry (Jibson et al., 1998, 2000) as  
105 below:

$$a_c = (F_S - 1)g \sin \alpha \quad (1)$$

106 where  $a_c$  is critical acceleration in terms of  $g$ , the acceleration due to earth's gravity,  $F_S$  is static factor  
107 of safety, and  $\alpha$  is the angle from the horizontal that the center of the slide block moves when  
108 displacement first occurs (Jibson et al., 1998, 2000). For a planar slip surface parallel to the slope, this  
109 angle can generally be approximated as the slope angle.

110 Natural slopes often develop a group of shallow unloading joints (Fig. 3) that parallel to the surface  
111 due to valley incisions (Gu, 1979; Hoek and Bray, 1981). Studies showed that rock slopes behave as  
112 collapsing and sliding failures of shallow unloading joints under strong earthquakes, and 90% of  
113 coseismic landslides are shallow falls and slides (Harp and Jibson, 1996; Khazai and Sitar, 2003; Dai et  
114 al., 2011; Tang et al., 2015). According to Qi et al. (2012), there are two typical kinds of earthquake  
115 triggered landslides, i.e., (a) shallow flow-like landslides with depth less than 3 m in general and (b) rock  
116 falls that are thrown by the earthquake shaking, usually occurred at the crest of the slope. For both types,  
117 the unstable rock blocks are often cut and activated along the rock joints. Therefore, the static factor of  
118 safety in terms of the critical acceleration in these conditions is related to the peak shear strength of the

119 rock joints. For the purpose of regional stable analysis, we use a limit-equilibrium model of an infinite  
 120 slope (Fig. 2) referring to the simplification of Jibson et al. (1998, 2000) on Newmark's method. On this  
 121 occasion, the value of the static factor of safety against sliding which is given by the ratio of resisting to  
 122 driving force is determined by conventional analysis with no consideration of accelerations, expressed as:

$$F_s = \frac{\text{Resisting force}}{\text{Driving force}} = \frac{\tau L}{mgsina} = \frac{\tau L}{\gamma Ltsina} = \frac{\tau}{\gamma tsina} \quad (2)$$

123 where  $\tau$  is peak shear strength of the rock joint,  $\gamma$  is unit weight of the rock mass, and  $t$  is the thickness  
 124 of the failure rock block.

125 For a Newmark analysis, it has been customary to describe the shear strength of rocks not rock joints  
 126 in terms of Coulomb's constants for friction and cohesion. However, both are not only stress dependent  
 127 variables, but also scale dependent (Barton and Choubey, 1977). According to Barton (1973), a more  
 128 satisfactory empirical relationship for predicting the peak shear strength of a joint can be written as  
 129 follows:

$$\tau = \sigma_n \tan [JRC \log_{10} \left( \frac{JCS}{\sigma_n} \right) + \phi_b] \quad (3)$$

130 where  $\sigma_n$  is effective normal stress,  $JRC$  is joint roughness coefficient,  $JCS$  is joint wall compressive  
 131 strength,  $\phi_b$  is basic friction angle, the angle of frictional sliding resistance between rock joints, which  
 132 can be obtained from residual shear tests on natural joints (Barton, 1973).

133 The effective normal stress ( $\sigma_n$ ) generated by the gravity acting on the rock block is as follows:

$$\sigma_n = \frac{mg \cos \alpha}{L} = \frac{\gamma L t \cos \alpha}{L} = \gamma t \cos \alpha \quad (4)$$

134 Considering the impact of size effect on  $JRC$  and  $JCS$ , formulations were developed by Barton and  
 135 Bandis (1982) and are shown as below:

$$JRC_n = JRC_0 \left( \frac{L_n}{L_0} \right)^{-0.02JRC_0} \quad (5)$$

$$JCS_n = JCS_0 \left( \frac{L_n}{L_0} \right)^{-0.03JRC_0} \quad (6)$$

136 where the nomenclature adopted incorporates the (0) and (n) for laboratory scale and in situ scale values  
 137 respectively.

138 Hence the static factor of safety ( $F_s$ ) of a slope can be written as:

$$\begin{aligned} F_s &= \frac{\tau}{\gamma t \sin \alpha} = \frac{\sigma_n \tan [JRC_n \log_{10} \left( \frac{JCS_n}{\sigma_n} \right) + \phi_b]}{\gamma t \sin \alpha} \\ &= \frac{\gamma t \cos \alpha \tan [JRC_n \log_{10} \left( \frac{JCS_n}{\gamma t \cos \alpha} \right) + \phi_b]}{\gamma t \sin \alpha} \\ &= \frac{\tan [JRC_n \log_{10} \left( \frac{JCS_n}{\gamma t \cos \alpha} \right) + \phi_b]}{\tan \alpha} \end{aligned} \quad (7)$$

139 After knowing the slope angle and the static factor of safety, the critical acceleration of a slope can  
 140 be determined. Once the earthquake acceleration-time history has been selected, those portions of the  
 141 record lying above the critical acceleration  $a_c$  (Fig. 4a) are integrated once to derive a velocity profile  
 142 (Fig. 4b), which in turn is integrated a second time to obtain the cumulative displacement profile of the  
 143 block (Fig. 4c), users then judge the dynamic performance of a slope based on the magnitude of the

144 Newmark displacement (Jibson et al., 1998, 2000; Jibson, 2011). The detailed procedure of conducting a  
145 Newmark analysis with Barton model is discussed in the following sections.

### 146 3.2 Static factor of safety

147 Considering that the mapped landslides greater than 1,000 m<sup>2</sup> occupy 96.1% of the total landslide area,  
148 we selected a 30 m×30 m digital elevation model (DEM), ASTER Global Digital Elevation Model  
149 (<https://doi.org/10.5067/ASTER/ASTGTM.002>, last accessed July 16, 2018) that is capable of facilitating  
150 the subsequent hazard analysis. A basic slope algorithm was applied to the DEM to produce a slope map  
151 (Fig. 5), where the slope is identified as the steepest downhill descent from the cell to its neighbors  
152 (Burrough and McDonnell, 1998). The slopes range from greater than 60° in the banks of the Niulanjiang  
153 River, the Shaba River and the Longquan River, to less than 20° in moderate and low mountains and hills  
154 in north and east.

155 For some slope steeper than 60°, few blocks can stay on that steep sliding surface, and the calculated  
156  $F_S$  will be nearly zero in this case. Actually, the unstable blocks have already failed, and further sliding  
157 will occur along a failure plane inside the slope, and the angle ( $\alpha$ ) of the inclination of the failure plane  
158 will be  $45^\circ + \frac{\phi_b}{2}$ . Therefore, we assigned an angle ( $\alpha$ ) of  $45^\circ + \frac{\phi_b}{2}$  to those slopes more than 60° to avoid a  
159 too low  $F_S$  in Newmark analysis.

160 Digital geologic map from China Geological Survey (GCS) was rasterized at 30 m grid spacing for  
161 assigning material properties throughout the study area. According to the literature researches, we found  
162 that  $JRC_0$  and  $JCS_0$  depend strongly on the lithology (Coulson, 1972; Barton and Choubey, 1977;  
163 Bandis et al., 1983; Priest, 1993; Bilgin and Pasamehmetoglu, 1990; Singh et al., 2012 Alejano et al.,

164 2012, 2014; Giusepone, 2014; Yong et al., 2018). Representative values of  $\gamma$ ,  $JRC_0$ ,  $JCS_0$  and  $\phi_b$   
165 assigned to each rock type exposed in the area can normally be estimated with the help of the test data  
166 listed in Table 1. The selected values were near the middle of the ranges represented in the references.  
167 These  $JRC_0$  and  $JCS_0$  are considered in laboratory scale, for the length of 100 mm as  $L_0$ . For each grid  
168 cell in regional analysis,  $L_n$ , the length of engineering dimension, can generally be set as a ten-fold range  
169 of  $L_0$ , because the value of  $JRC_n/JRC_0$  ( $JCS_n/JCS_0$ ) is almost constant when the value of  $L_n/L_0$   
170 greater than 10 (Bandis et al., 1981). The values of  $JRC_n$  and  $JCS_n$ , then, are calculated by inserting  
171 values from  $JRC_0$ ,  $JCS_0$ ,  $L_0$ , and  $L_n$  into Eq. (5) and Eq. (6). Fig. 6a and Fig. 6b show the spatial  
172 distribution of  $JRC_n$  and  $JCS_n$  respectively. The basic-friction-angle ( $\phi_b$ ) map and unit weight ( $\gamma$ ) map  
173 are shown as Fig. 7 and Fig. 8 respectively.

174 For simplicity, the thickness of the modeled block  $t$  was taken to be 3 m, which reflects the typical  
175 slope failures of the Ludian earthquake. The static factor-of-safety map was produced by combing these  
176 data layers ( $\alpha$ ,  $JRC_n$ ,  $JCS_n$ ,  $\phi_b$ , and  $\gamma$ ) in Eq. (7). In the initial iteration of the calculation, grid cells in  
177 steep areas with static factors of safety less than 1 indicate that the slopes are statically unstable, but do  
178 not necessarily mean that the slopes are moving under the earthquake shaking. In this condition, to avoid  
179 conservative results, we did not increase the strengths of rock types having statically unstable cells, either,  
180 adjust strengths of other rock types to preserve the relative strength differences between rock types (Jibson  
181 et al., 1998, 2000). Instead we assigned a minimal static factor of safety as 1.01, merely above limit  
182 equilibrium (Jibson et al., 1998, 2000), to these slopes, to avoid a negative value of the critical acceleration  
183  $a_c$ . According to Keefer (1984), most landslides triggered by earthquakes occur with a slope of  $5^\circ$  at least.  
184 Static factors of safety resulting from slopes less than  $5^\circ$  were very high, and these slopes that were

185 ~~impossible to have failures~~ under the Ludian earthquake did not produce a statistically significant sample  
186 ~~to the~~ analysis. Therefore, slopes less than  $5^\circ$  were not analyzed during the second iteration. After the  
187 adjustment, the static factors of safety ranged from 1.0 to 17.4, as shown in Fig. 9. 

### 188 3.3 Critical acceleration

189 According to Newmark (1965), a pseudostatic analysis in terms of the static factor of safety and the  
190 slope angle was employed to calculate the critical acceleration of a potential landslide. The critical-  
191 acceleration map (Fig. 10) was produced by combining the static factor of safety and the slope angle in  
192 Eq. (1).

193 The critical acceleration that results in a static factor of safety of 1.0 and initiates a sliding of a slope in  
194 a limit-equilibrium analysis is derived from the intrinsic slope properties (topography and lithology),  
195 regardless which ground shaking is given. Therefore, the critical-acceleration map indicates the  
196 susceptibility of the coseismic landslides (Jibson et al., 1998, 2000). The calculated critical accelerations  
197 range from almost zero in areas that are more susceptible to coseismic landslides, to  $14.0 g$  in areas with  
198 lower susceptibility. 

### 199 3.4 Shake map

200 There are 23 strong-motion stations within 100 km of the Ludian earthquake epicenter (Fig. 11).  
201 Each station record includes three components of the peak ground acceleration (*PGA*), in south-north  
202 direction, east-west direction and up-down direction respectively, as listed in Table 2 (The data set is  
203 provided by China Earthquake Data Center, <http://data.earthquake.cn>, last accessed June 16, 2016). We  
204 calculated the average *PGA* of the two horizontal components of each strong-motion recording, and then  
205 plotted a contour map (Fig. 12) using an Inverse Distance Weighted (IDW) interpolation algorithm. This 

206 ~~method assumes that the variable of the average  $PGA$  being mapped decreases in influence with distance~~  
207 ~~from its sampled location. Inverse Distance Weighted (IDW) interpolation~~ determines cell values using a  
208 linearly weighted combination of a set of sample stations (Watson and Philip, 1985). The weight is a  
209 ~~function of inverse~~ distance. In addition, considering that input stations far away from the epicenter  
210 location where the prediction is being made may have poor or no spatial correlation, we eliminated the  
211 input stations out of 100 km from the calculation.

### 212 3.5 Newmark displacement

213 In a real landslide hazard case, it is impossible to conduct a rigorous Newmark analysis when  
214 accelerometer records are unavailable. It is also impractical and time consuming to produce a  
215 displacement in each cell during the regional analysis. Therefore, empirical regressions (Ambraseys and  
216 Menu, 1988; Bray and Travararou, 2007; Jibson, 2007; Saygili and Rathje, 2008; Rathje and Saygili,  
217 2009; Hsieh and Lee, 2011) were proposed to estimate Newmark displacement as a function of the critical  
218 acceleration and peak ground acceleration or Arias intensity. Among those empirical estimations, Rathje  
219 and Saygili (2009) developed a vector model for displacement in terms of the critical acceleration ( $a_c$ ),  
220 peak ground acceleration ( $PGA$ ) and moment magnitude ( $M_w$ ) based on analysis of over 2,000 strong  
221 motions.

$$\begin{aligned} \ln D = & 4.89 - 4.85 \left( \frac{a_c}{PGA} \right) - 19.64 \left( \frac{a_c}{PGA} \right)^2 + 42.49 \left( \frac{a_c}{PGA} \right)^3 - 29.06 \left( \frac{a_c}{PGA} \right)^4 \\ & + 0.72 \ln (PGA) + 0.89(M_w - 6) \end{aligned} \quad (8)$$

222 where  $D$  is predicted displacement in units of  $cm$ ,  $a_c$  and  $PGA$  are in units of  $g$ .

223 This model is a preferred displacement model at a specific site where acceleration-time recordings are  
224 not available. The incorporating multiple ground motion parameters in the analysis typically results in  
225 less variability in the prediction of displacement (Rathje and Saygili, 2009).

226 The Newmark displacement (Fig. 13) in each cell was calculated by combing corresponding values  
227 of the critical acceleration, peak ground acceleration and moment magnitude in Eq (8). Predicted  
228 displacements range from 0 cm to 122 cm.

### 229 3.6 Certainty factor and coseismic landslide hazard map

230 According to Jibson et al. (1998, 2000), predicted displacements provide an index of seismic  
231 performance of slopes, larger predicted displacements relate to greater incidence of slope failures. But the  
232 displacements do not correspond directly to measurable slope movements in the field. To produce a  
233 coseismic landslide hazard map, we chose a model of inexact reasoning, the certainty factor model (CFM),  
234 which was created by Shortliffe and Buchanan (1975) and improved by Hecheran (1986), to explore  
235 the relationship between the landslide occurrences and the predicted displacements. The CFM was created  
236 as a numerical method, which was initially used by MYCIN, a backward chaining expert system in  
237 medicine (Shortliffe and Buchanan, 1975), for managing uncertainty in a rule-based system. In this model,  
238 the certainty factor  $CF$  represents the net confidence in a hypothesis  $H$  based on the evidence  $E$   
239 (Hecheran, 1986). Certainty factors range between -1 and 1. A  $CF$  with a value of -1 means total lack  
240 of confidence, whereas a  $CF$  with a value of 1 means total confidence. Values greater than 0 favor the  
241 hypothesis while values less than 0 favor the negation of the hypothesis. According to Hecheran (1986),  
242 there is a probabilistic interpretation for  $CF$  shown as below:

$$CF = \begin{cases} \frac{p(H|E) - p(H)}{p(H|E)[1 - p(H)]}, & p(H|E) > p(H) \\ \frac{p(H|E) - p(H)}{p(H)[1 - p(H|E)]}, & p(H|E) < p(H) \end{cases} \quad (9)$$

243 where  $CF$  is the certainty factor,  $p(H|E)$  denotes the conditional probability for the case of a posterior  
 244 hypothesis that relies on evidence, the posterior probability, and  $p(H)$  is the prior probability before any  
 245 evidence is known. In the displacement analysis,  $p(H|E)$  was defined as the proportion of the landslide  
 246 area within a specific displacement area while  $p(H)$  was defined as the proportion of the landslide area  
 247 within the entire study area excluding the slopes less than  $5^\circ$ . In this way, values of  $CF$  represent the  
 248 confidence level of coseismic landslides. Positive values correspond to an increase in confidence level in  
 249 a slope failure while negative quantities correspond to a decrease in confidence level. Greater positive  
 250 values indicate higher confidence level of coseismic landslides.

251 Given this definition, we could produce a coseismic landslide hazard map in terms of certainty factors.  
 252 First, displacement cells in every 1 cm were grouped into bins, such that all cells having displacements  
 253 between 0 cm and 1 cm were grouped into the first bin; those having displacements between 1 cm and 2  
 254 cm were grouped into the second bin, and so on. The displacements were grouped into 123 bins, from 0  
 255 cm to 122 cm. Later, we calculated the proportion of cells occupied by landslide area in each bin. This  
 256 proportion was considered the posterior probability of each bin as defined. The prior probability  
 257 calculated by dividing the entire landslide area by the entire study area is same in each bin. Finally, values  
 258 of  $CF$  were computed in each bin by using Eq. (9) to combine corresponding values of the posterior  
 259 probability and prior probability. Certainty factors range from -1 to 0.95. Values of  $CF$  indicate the

260 confidence level of landslide occurrence of each bin in the study area and provide the basis for producing  
261 a coseismic landslide hazard map.

262 As shown in the hazard map for the Ludian earthquake (Fig. 14), most of the actual triggered landslides  
263 lie in the higher confidence-level areas with  $CF$  values greater than 0.60. The interpreted landslides are  
264 covered on the map to demonstrate the good fit for predicted confidence levels of coseismic landslides.

265

#### 266 **4. Results and Discussion**

267 The predicted displacements represent the cumulative sliding displacements for a given  
268 acceleration-time history. Based on the statistically significant sizes of the area of each displacement,  
269 displacements less than 60 cm, which is around the middle of the displacement range, occupy about 80%  
270 of the study area, while displacements greater than 80 cm occupy a very small area. Jibson et al. (1998,  
271 2000) supposed that shallow falls and slides in brittle, weakly cemented materials would fail at a relatively  
272 small displacement, while slumps and block slides in more compliant materials would likely fail at a  
273 larger displacement. That is to say, the study area is more susceptible to rock falls and shallow, disrupted  
274 slides that fail at a relatively small displacement, while the study area is with a lower probability subjected  
275 to coherent, deep-seated slides that would fail at a larger displacement. Indeed, the majority of landslides  
276 triggered by the Ludian earthquake were shallow, disrupted slides and rock falls (Zhou et al., 2016).  
277 Although few catastrophic rock avalanches, such as the Hongshiyuan landslide (Chang et al., 2017),  
278 occurred in the field, they did not produce statistically significant samples that could meaningfully  
279 contribute to the model, which was consistent with the statistic results as discussed previously. Therefore,

280 the model should relate well to typical kinds of earthquake-induced landslides in the study area,  
281 meanwhile demonstrate its potential utility to predict the probability of other types of landslides.

282 For each  $CF$ -value area, the proportion of area occupied by landslide area was plotted as a dot in 

283 **Fig. 15.** The data was fitted by a piecewise function, which was derived from Eq. (9). Different from a  
284 Weibull curve (1939) through statistical regression, whose shape would probably be different in different  
285 regions (Jibson et al., 1998, 2000), the piecewise function of  $CF$  value and the proportion of landslide  
286 area can be derived from Eq. (9). This method is more universal. From the curve shown in Fig. 15, when  
287 the value of  $CF$  is reaching 1.0 (total confidence), the proportion of landslide area is trending to  
288 monotonically increase, which means the confidence level of a slope failure is growing and a landslide  
289 would probably occur. Such a procedure is consistent with the interpretation of the certainty factor theory.  
290 Therefore, the CFM demonstrates the capability of its representation and predicting approach for a  
291 probabilistic hazard analysis of coseismic landslides.

292 When fitting the results of shear tests using Coulomb's linear relation, the shear strengths vary widely  
293 from high normal stress in laboratory to low normal stress in the field (Barton, 1973). We introduced  
294 Barton model into the Newmark analysis to reduce the variability of shear strengths in terms of Coulomb's  
295 constants. And we considered the impact of scale effects by using Eq. (5) and Eq. (6), which helps to  
296 prevent Newmark's method from underestimating the shear strength of geologic units in a regional  
297 analysis. In addition, for Barton model, the joint roughness coefficient ( $JRC$ ) could be estimated from tilt  
298 tests or from matching of Barton joint standard roughness profiles that were regarded by the International  
299 Society for Rock Mechanics (ISRM, 1978), while the joint wall compressive strength ( $JCS$ ) could be  
300 estimated by Schmidt hammer index tests. These tests are helpful to make a quick estimate of the shear

301 strength in situ, which could facilitate using Newmark's method in an emergency hazard and risk  
302 assessment after an earthquake.

303 It is difficult for a statically stable slope to fail under an earthquake. Earthquakes usually make statically  
304 unstable slopes or slopes on the boundary fail. For this reason, it is important to truthfully characterize  
305 the shear strengths of slopes. Shear strengths assigned to the geologic units were from results of hundreds  
306 of shear tests from the references. We assigned the original shear strengths to the geologic units other than  
307 increasing strengths to make statically unstable cells stable as Jibson et al. (1998, 200) did, which will  
308 change the statically stable level of the whole area, especially the slopes on the boundary at first. In  
309 addition, we considered size effect of the potential slide surface, this would yield lower  $F_S$ , which, in turn,  
310 yield higher displacement. However, the actual inventory of landslides was used to calibrate the predicted  
311 displacements, and the confidence levels indicated by certainty factors fit well of the spatial distribution  
312 of coseismic landslides as shown in the hazard map (Fig. 14).

313 We also ran a conventional Newmark analysis using assigned strengths, such as internal friction angle  
314 ( $\phi$ ) and cohesion ( $c$ ) as shown in Table 2. Predicted displacements calculated by the conventional  
315 Newmark analysis range from 0 cm to 121 cm, compared with 0 cm to 122 cm by the new method  
316 described in the paper. Fig. 16 shows the hazard map produced using the conventional Newmark analysis.  
317 The  $CF$ s range from -1 to 0.94, almost the same as results from the new method above. However, there  
318 are big differences along the Shaba River and upstream of the Niulanjiang River from these two methods.  
319 By comparing Fig. 14 with Fig. 16, we can see that confidence levels from the new method fit better than  
320 that of the conventional method, especially near upstream of the Niulanjiang River. The area under the  
321 curve (AUC) analysis was employed to compare performances of both methods. To create an AUC plot,

322 the cumulative area of *CFs* within each interval of calculated values from the maximum to the minimum  
323 was determined as a proportion of the total study area (x-axis) and plotted against the proportion of  
324 cumulative landslides falling within those *CFs* (y-axis) (Miles and Keefer, 2009). The area under the  
325 curve is calculated as an index to conduct comparison across both methods. A value of 0.5 indicates  
326 performance that is no better than random guessing and 1.0 indicates perfect performance (Miles and  
327 Keefer, 2009). Fig. 17 shows the results of the AUC analysis for both methods. The calculated AUC value  
328 for the new method is 0.58, while the value for the conventional Newmark's method is 0.53. That is to  
329 say, the new method introduced in this paper yields better results, and it is actually an improvement over  
330 the conventional way of Newmark analysis.

331

## 332 **5. Conclusion**

333 Newmark's method is a useful, physically based model to estimate the seismic stability of natural slopes.  
334 Mapping procedure of data from the 2014 Ludian earthquake shows the feasibility of a Newmark analysis  
335 combined with Barton' shear strength criterion. Such method provides practical applications in regional  
336 seismic hazard assessment. We also consider the size effect of shear strength parameters, such as the joint  
337 roughness coefficient (*JRC*) and the joint wall compressive strength (*JCS*) in a regional analysis. Moreover,  
338 the linkage of Newmark displacements to certainty factor model improves the utility of Newmark's  
339 method to predict the hazard of coseismic landslides. Finally, results of the AUC analysis indicate that the  
340 new method has higher reliability than a conventional Newmark's method.

341

## 342 **Acknowledgements**

343           This work is supported by Natural Science Foundation of China under Grants of Nos. 41825018 and  
344 41672307, Science and Technology Service Network Initiative under Grant No. KFJ-EW-STS-094, and  
345 the sponsorship from the China Scholarship Council (No. 201704910537).

346

347 **References**

- 348 Alejano, L. R., González, J. and Muralha, J.: Comparison of different techniques of tilt testing and basic  
349 friction angle variability assessment. *Rock mechanics and rock engineering* 45(6), 1023-1035, 2012.
- 350 Alejano, L. R., Perucho, Á., Olalla, C. and Jiménez, R.: *Rock engineering and rock mechanics: structures*  
351 *in and on rock masses*. CRC Press, Boca Raton, Florida, 615-1148, 2014.
- 352 Ambraseys, N. N. and Menu, J. M.: Earthquake-induced ground displacements. *Earthquake engineering*  
353 *and structural dynamics* 16(7), 985-1006, 1988.
- 354 Bandis, S., Lumsden, A. C. and Barton, N. R.: Experimental studies of scale effects on the shear behaviour  
355 of rock joints. *International Journal of Rock Mechanics and Mining Sciences & Geomechanics*  
356 *Abstracts* 18(1), 1-21, 1981.
- 357 Bandis, S. C., Lumsden, A. C. and Barton, N. R.: Fundamentals of rock joint deformation. *International*  
358 *Journal of Rock Mechanics and Mining Sciences & Geomechanics Abstracts* 20(6), 249-268, 1983.
- 359 Barton, N.: Review of a new shear-strength criterion for rock joints. *Engineering geology* 7(4), 287-332,  
360 1973.
- 361 Barton, N. and Bandis, S.: Effects of block size on the shear behavior of jointed rock. Keynote Lecture in  
362 the 23rd US Symposium on Rock Mechanics (USRMS). American Rock Mechanics Association,  
363 Berkeley, California, 739-760, 1982.
- 364 Barton, N. and Choubey, V.: The shear strength of rock joints in theory and practice. *Rock mechanics*  
365 10(1-2), 1-54, 1977.
- 366 Bilgin, H. A. and Pasamehmetoglu, A. G.: Shear behaviour of shale joints under heat in direct shear. In  
367 Barton N. and Stephansson O. (Eds.), *Rock joints*. CRC Press, Rotterdam, 179-183, 1990.

368 Bray, J. D. and Travasarou, T.: Simplified procedure for estimating earthquake-induced deviatoric slope  
369 displacements. *Journal of geotechnical and geoenvironmental engineering* 133(4), 381-92, 2007.

370 Burrough, P. A. and McDonnell, R. A.: *Principles of geographical information systems (2nd Edition)*.  
371 Oxford University Press, New York, 190, 1998.

372 Chang, Z. F., Chang, H., Yang, S. Y., Chen, G. and Li, J. L.: Characteristics and formation mechanism of  
373 large rock avalanches triggered by the Ludian Ms6.5 earthquake at Hongshiyan and Ganjiazhai.  
374 *Seismology and Geology* 39(5), 1030-1047, 2017 (in Chinese with English abstract).

375 Chen, X. L., Ran, H. L. and Yang, W. T.: Evaluation of factors controlling large earthquake-induced  
376 landslides by the Wenchuan earthquake. *Natural Hazards and Earth System Sciences*, 12(12), 3645-  
377 3657, 2012.

378 Chen, X. L., Zhou, Q. and Liu, C. G.: Distribution pattern of coseismic landslides triggered by the 2014  
379 Ludian, Yunnan, China Mw6.1 earthquake: special controlling conditions of local topography.  
380 *Landslides* 12(6), 1159-1168, 2015.

381 Chen, X. L., Liu, C. G., Wang, M. M. and Zhou, Q.: Causes of unusual distribution of coseismic landslides  
382 triggered by the Mw 6.1 2014 Ludian, Yunnan, China earthquake. *Journal of Asian Earth Sciences* 159,  
383 17-23, 2018.

384 Chen, X. L., Liu, C. G. and Wang, M. M.: A method for quick assessment of earthquake-triggered  
385 landslide hazards: a case study of the Mw6. 1 2014 Ludian, China earthquake. *Bulletin of Engineering*  
386 *Geology and the Environment* 78(4), 2449-2458, 2019.

387 Clough, R. W. and Chopra, A. K.: Earthquake stress analysis in earth dams. *ASCE Journal of the*  
388 *Engineering Mechanics Division* 92, 197-211, 1966.

389 Coulson, J.H.: Shear strength of flat surfaces in rock. In Cording, E. J. (Ed.), Stability of Rock Slopes.  
390 13th Symposium on Rock Mechanics, Urbana, Illinois, 77-105, 1972.

391 Dai, F. C., Xu, C., Yao, X., Xu, L., Tu, X. B. and Gong, Q. M.: Spatial distribution of landslides triggered  
392 by the 2008 Ms 8.0 Wenchuan earthquake, China. Journal of Asian Earth Sciences 40(4), 883-895,  
393 2011.

394 Geological Engineering Handbook Editorial Committee: Geological Engineering Handbook. China  
395 Architecture & Building Press, Beijing, 2018 (in Chinese).

396 Giusepone, F. and da Silva, L. A. A.: Hoek & Brown and Barton & Bandis Criteria Applied to a Planar  
397 Sliding at a Dolomite Mine in Gandarela Synclinal. In ISRM Conference on Rock Mechanics for  
398 Natural Resources and Infrastructure-SBMR 2014. International Society for Rock Mechanics, 2014.

399 Gu, D. Z.: Engineering geomechanics of rock mass. Science Press, Beijing, China, 1979 (in Chinese).

400 Harp, E. L. and Jibson, R. W.: Landslides triggered by the 1994 Northridge, California, earthquake.  
401 Bulletin of the Seismological Society of America 86(1B), S319-S332, 1996.

402 Heckerman, D.: Probabilistic interpretations for MYCIN's certainty factors. In Kanal, L. N. and Lemmer,  
403 J. F. (Eds), Machine Intelligence and Pattern Recognition 4, North-Holland, 167-196, 1986.

404 Hsieh, S. Y. and Lee, C. T.: Empirical estimation of the Newmark displacement from the Arias intensity  
405 and critical acceleration. Engineering Geology 122(1-2), 34-42, 2011.

406 Hoek, E. and Bray, J. D.: Rock slope engineering. CRC Press, 1981.

407 ISRM (International Society for Rock Mechanics): Suggested Methods for the Quantitative Description  
408 of Discontinuities in Rock Masses. International Journal of Rock Mechanics and Mining Sciences &  
409 Geomechanics Abstracts 15, 319-368, 1978.

410 Jibson, R. W.: Predicting earthquake-induced landslide displacements using Newmark's sliding block  
411 analysis. Transportation research record 1411, 9-17, 1993.

412 Jibson, R. W.: Methods for assessing the stability of slopes during earthquakes-A retrospective.  
413 Engineering Geology, 122(1-2), 43-50, 2011.

414 Jibson, R. W.: Regression models for estimating coseismic landslide displacement. Engineering Geology  
415 91(2), 209-218, 2007.

416 Jibson, R. W., Harp, E. L. and Michael, J. A.: A method for producing digital probabilistic seismic  
417 landslide hazard maps: an example from the Los Angeles, California, area. US Geological Survey.  
418 Open-File Rep. 98-113. 17 pp., 1998.

419 Jibson, R. W., Harp, E. L. and Michael, J. A.: A method for producing digital probabilistic seismic  
420 landslide hazard maps. Engineering Geology 58(3-4), 271-289, 2000.

421 Keefer, D. K.: Landslides caused by earthquakes. Geological Society of America Bulletin 95(4), 406-421,  
422 1984.

423 Khazai, B. and Sitar, N.: Evaluation of factors controlling earthquake-induced landslides caused by Chi-  
424 Chi earthquake and comparison with the Northridge and Loma Prieta events. Engineering geology  
425 71(1-2), 79-95, 2004.

426 Miles, S. B. and Keefer, D. K.: Evaluation of CAMEL—comprehensive areal model of earthquake-  
427 induced landslides. Engineering Geology 104(1-2), 1-15, 2009.

428 NASA/METI/AIST/Japan Spacesystems and U.S./Japan ASTER Science Team: ASTER Global Digital  
429 Elevation Model version 2. NASA EOSDIS Land Processes DAAC, [https://doi:  
430 10.5067/ASTER/ASTGTM.002](https://doi:10.5067/ASTER/ASTGTM.002) (last accessed July 16, 2018), 2009.

431 Newmark, N. M.: Effects of earthquakes on dams and embankments. *Geotechnique* 15(2), 139-160, 1965.

432 Pradel, D., Smith, P. M., Stewart, J. P. and Raad, G.: Case history of landslide movement during the  
433 Northridge earthquake. *Journal of Geotechnical and Geoenvironmental Engineering* 131(11), 1360-  
434 1369, 2005.

435 Priest, S. D.: *Discontinuity analysis for rock engineering*. Springer Science & Business Media, B.V.,  
436 Dordrecht, 320, ~~2012~~.

437 Qi, S. W., Xu, Q., Lan, H. X., Zhang, B. and Liu, J. Y.: Spatial distribution analysis of landslides triggered  
438 by 2008.5.12 Wenchuan Earthquake, China, *Engineering Geology* 116 (1-2), 95~108, 2010.

439 Qi, S. W., Xu, Q., Zhang, B., Zhou, Y. D., Lan, H. X. and Li, L. H.: Source characteristics of long runout  
440 rock avalanches triggered by the 2008 Wenchuan earthquake, China, *Journal of Asian Earth Sciences*  
441 40 (4), 896~906, 2011.

442 Qi, S. W., Yan, C. G. and Liu, C. L.: Two typical types of earthquake triggered landslides and their  
443 mechanisms. In *Landslides and Engineered Slopes: Protecting Society through Improved*  
444 *Understanding*, ISBN 978-0-415-63303-1, 2012.

445 Rathje, E. M. and Antonakos, G.: A unified model for predicting earthquake-induced sliding  
446 displacements of rigid and flexible slopes. *Engineering Geology* 122(1-2), 51-60, 2011.

447 Rathje, E. M. and Saygili, G.: Probabilistic assessment of earthquake-induced sliding displacements of  
448 natural slopes. *Bulletin of the New Zealand Society for Earthquake Engineering* 42(1), 18-27, 2009.

449 Saygili, G. and Rathje, E. M.: Empirical predictive models for earthquake-induced sliding displacements  
450 of slopes. *Journal of Geotechnical and Geoenvironmental Engineering* 134(6), 790-803, 2008.

451 Shortliffe, E. H. and Buchanan, B. G.: A model of inexact reasoning in medicine. *Mathematical*  
452 *Biosciences* 23, 351-379, 1975.

453 Singh, T. N., Kainthola, A. and Venkatesh, A.: Correlation between point load index and uniaxial  
454 compressive strength for different rock types. *Rock Mechanics and Rock Engineering* 45(2), 259-264,  
455 2012.

456 Tang, C., Ma, G., Chang, M., Li, W., Zhang, D., Jia, T. and Zhou, Z.: Landslides triggered by the 20 April  
457 2013 Lushan earthquake, Sichuan Province, China. *Engineering Geology* 187, 45-55, 2015.

458 [Terzaghi](#), K.: Mechanism of landslides. In Paige, S. (Ed.), *Application of Geology to Engineering Practice*  
459 (Berkey Volume). Geological Society of America, New York, NY, 83-123, 1950.

460 Watson, D. F. and Philip, G. M.: A Refinement of Inverse Distance Weighted Interpolation. *Geoprocessing*  
461 2, 315–327, 1985.

462 Weibull, W.: In: *A Statistical Theory of the Strength of Materials*. Ingenioersvetenskaps-akademien,  
463 Handlingar, Stockholm, p., 151, 1939.

464 Wieczorek, G. F., Wilson, R. C. and Harp, E. L.: Map showing slope stability during earthquakes in San  
465 Mateo County, California. U.S. Geological Survey Miscellaneous Investigations Map I-1257-E, scale  
466 1:62,500, 1985.

467 Wilson, R. C. and Keefer, D. K.: Dynamic analysis of a slope failure from the 6 August 1979 Coyote  
468 Lake, California, earthquake. *Bulletin of the Seismological Society of America* 73(3), 863-877, 1983.

469 Xu, C., Xu, X., Zhou, B., and Yu, G.: Revisions of the M 8.0 Wenchuan earthquake seismic intensity  
470 map based on co-seismic landslide abundance. *Natural Hazards*, 69(3), 1459-1476, 2013.

471 Yong, R., Ye, J., Liang, Q. F., Huang, M. and Du, S. G.: Estimation of the joint roughness coefficient  
472 (JRC) of rock joints by vector similarity measures. *Bulletin of Engineering Geology and the*  
473 *Environment* 77, 735-749, 2018.

474 Yuan, R. M., Tang, C. L., Hu, J. C., and Xu, X. W.: Mechanism of the Donghekou landslide triggered by  
475 the 2008 Wenchuan earthquake revealed by discrete element modeling. *Natural Hazards and Earth*  
476 *System Sciences*, 14(5), 1195-1205, 2014.

477 Zhou, S. H., Chen, G. Q. and Fang, L. G.: Distribution pattern of landslides triggered by the 2014 Ludian  
478 earthquake of China: Implications for regional threshold topography and the seismogenic fault  
479 identification. *ISPRS International Journal of Geo-Information* 5(4), 46, 2016.

480

481 **Figure Captions**

482 **Fig. 1.** Map of the study area showing interpreted landslides.

483 **Fig. 2.** Conceptual sliding-block model of a Newmark analysis.

484 **Fig. 3.** A schematic diagram showing shadow unloading joints in the slope.

485 **Fig. 4.** Demonstration of the Newmark-analysis algorithm (adapted from [Wilson and Keefer, 1983](#); [Jibson](#)  
486 [et al., 1998, 2000](#))

487 **Fig. 5.** Slope map derived from the DEM of the study area.

488 **Fig. 6.** (a)  $JRC_n$  component and (b)  $JCS_n$  component of shear strength assigned to rock types in the  
489 study area.

490 **Fig. 7.** Basic-friction-angle ( $\phi_b$ ) component of shear strength assigned to rock types in the study area.

491 **Fig. 8.** Unit weight ( $\gamma$ ) assigned to rock types in the study area.

492 **Fig. 9.** Static factor-of-safety map of the study area.

493 **Fig. 10.** Map showing critical accelerations in the study area.

494 **Fig. 11.** Locations of strong-motion stations.

495 **Fig. 12.** Contour map of peak ground acceleration ( $PGA$ ) produced by the Ludian earthquake in the  
496 study area.  $PGA$  values shown are in  $g$ .

497 **Fig. 13.** Map showing predicted displacements in the study area.

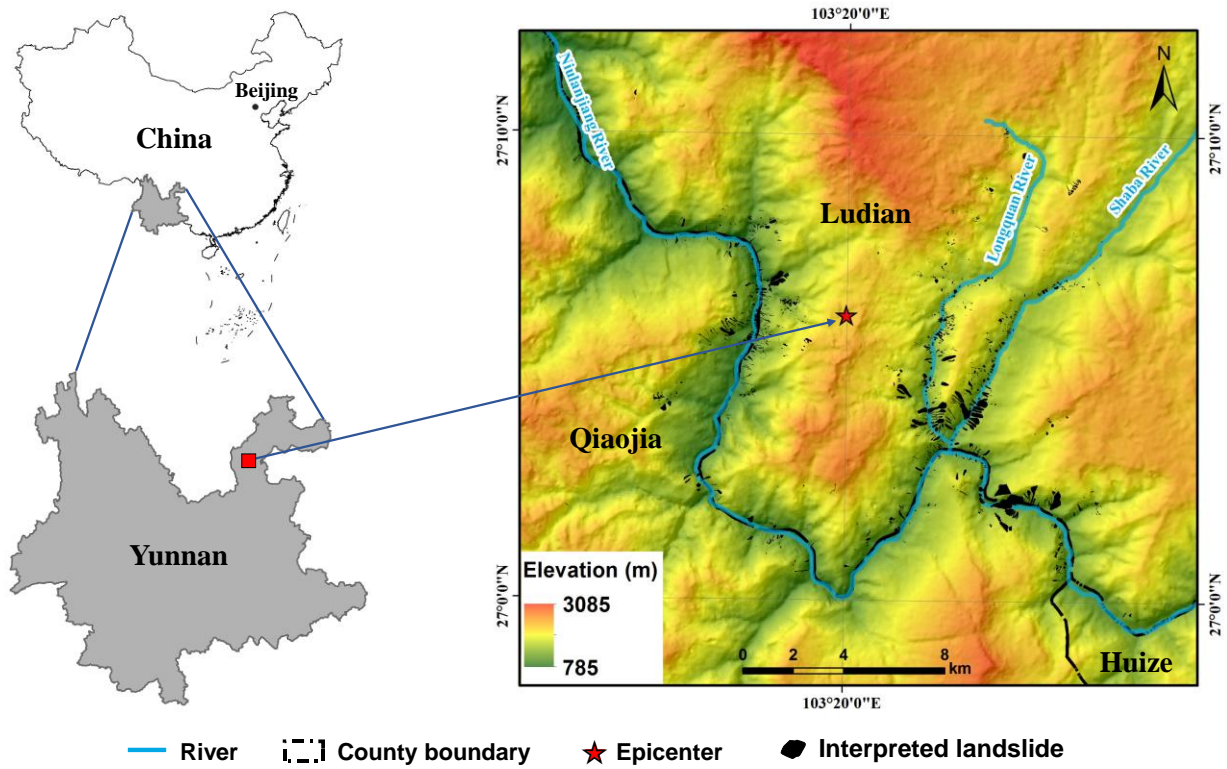
498 **Fig. 14.** Map showing confidence levels of coseismic landslides in the Ludian earthquake using method  
499 introduced in this paper. Confidence levels are portrayed in terms of values of  $CF$ .

500 **Fig. 15.** Proportion of the area of landslides lying in each  $CF$ -value area. A dot shows the proportion of  
501 landslide area within an area of  $CF$  value; the red line is the fitting curve of the data using second order  
502 exponential growth function.

503 **Fig. 16.** Map showing confidence levels of coseismic landslides in the Ludian earthquake using a  
504 conventional Newmark analysis. Confidence levels are portrayed in terms of values of  $CF$ .

505 **Fig. 17.** Area under the curve plots for comparing the new method with a conventional Newmark's  
506 method.

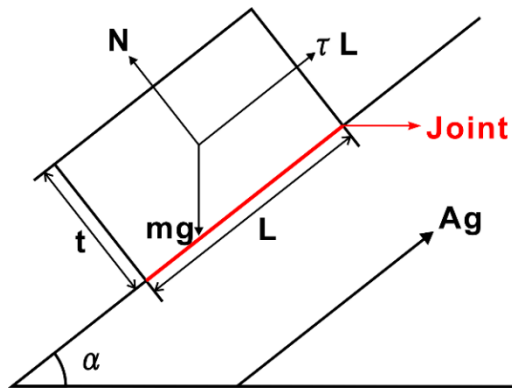
507



508

509 **Fig. 1.** Map of the study area showing interpreted landslides.

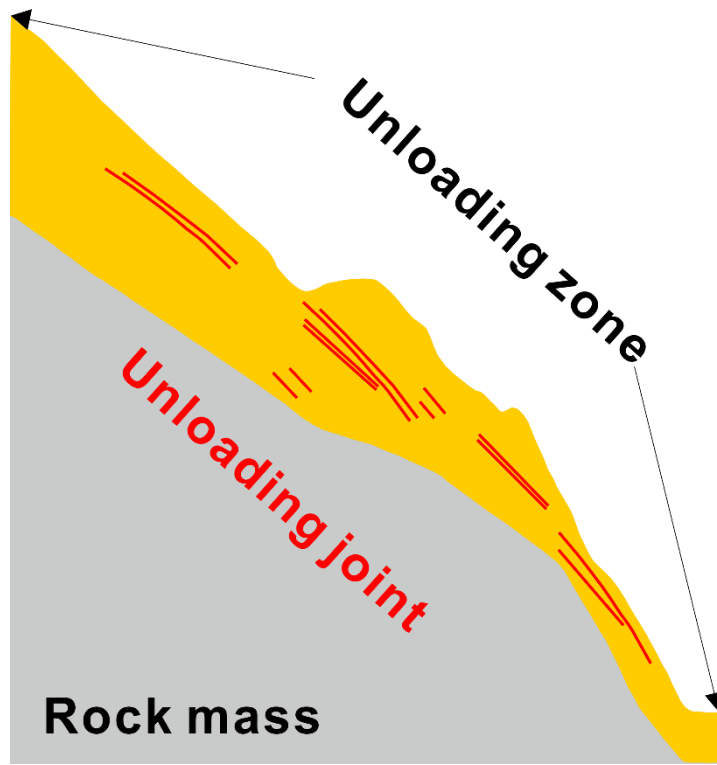
510



511

512 **Fig. 2.** Conceptual sliding-block model of a Newmark analysis. The potential landslide is modeled as a  
 513 rigid-plastic block resting on an inclined plane at an angle ( $\alpha$ ) from the horizontal (Jibson et al., 1998,  
 514 2000). The base of the block is subjected to an earthquake ground acceleration that is denoted by  $Ag$ .

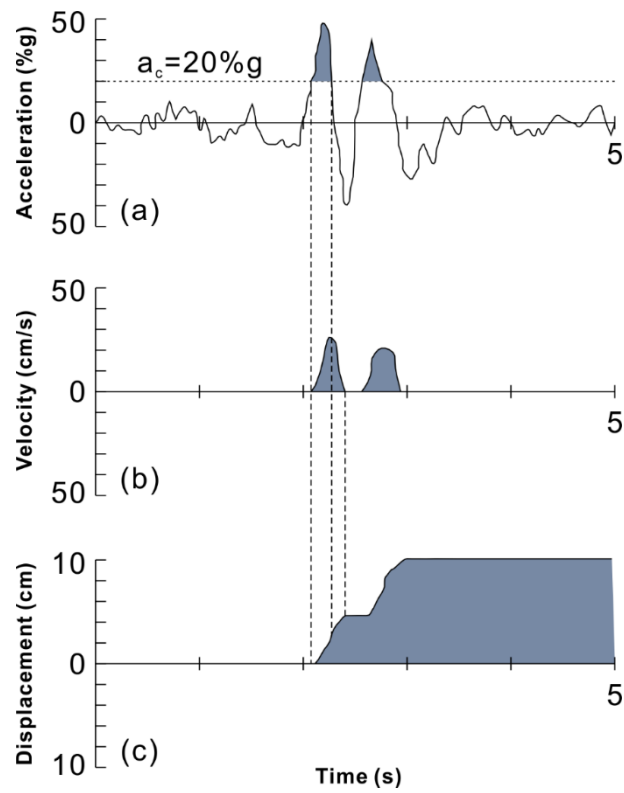
515



516

517 **Fig. 3.** A schematic diagram showing shallow unloading joints in the slope.

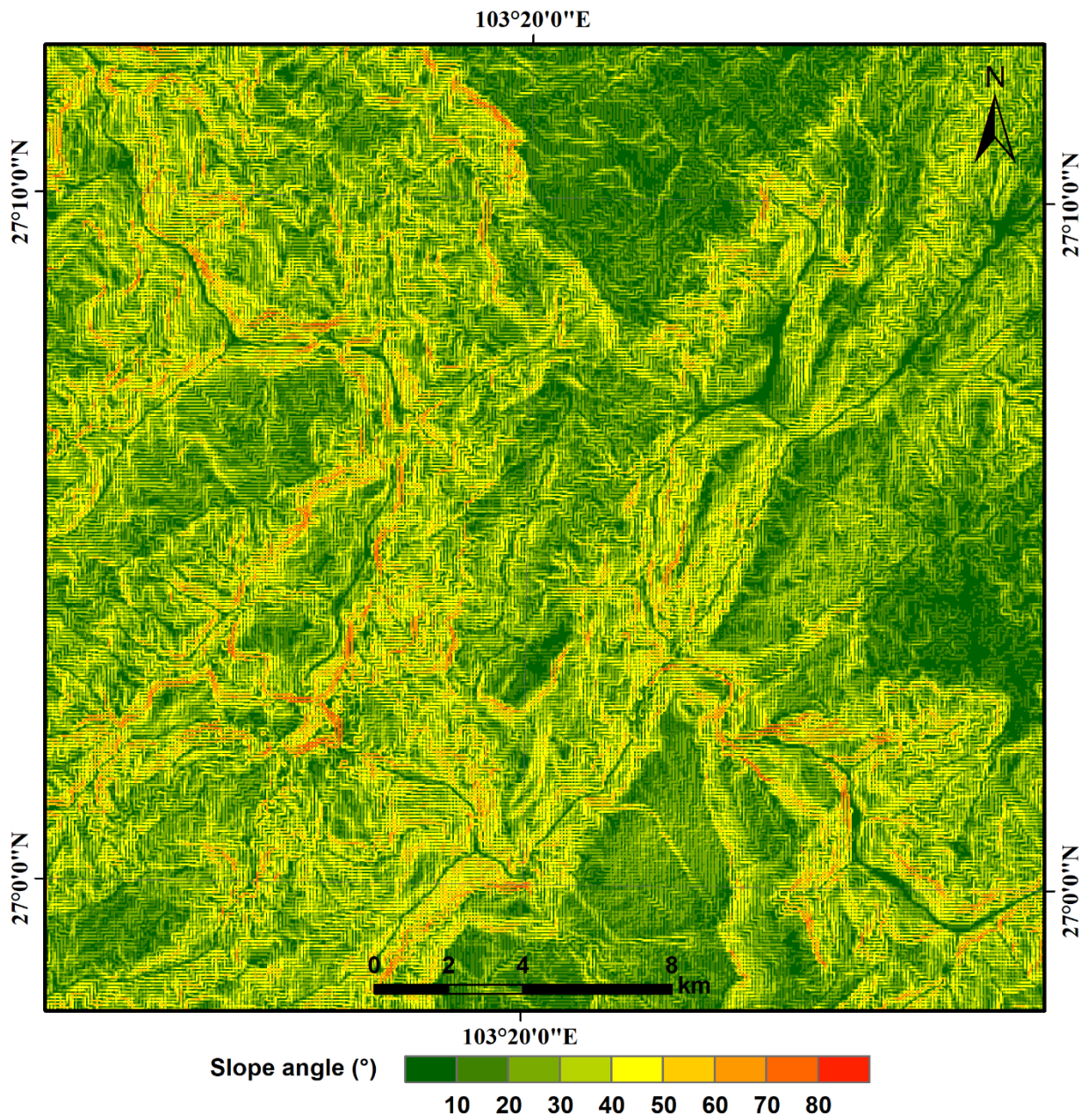
518



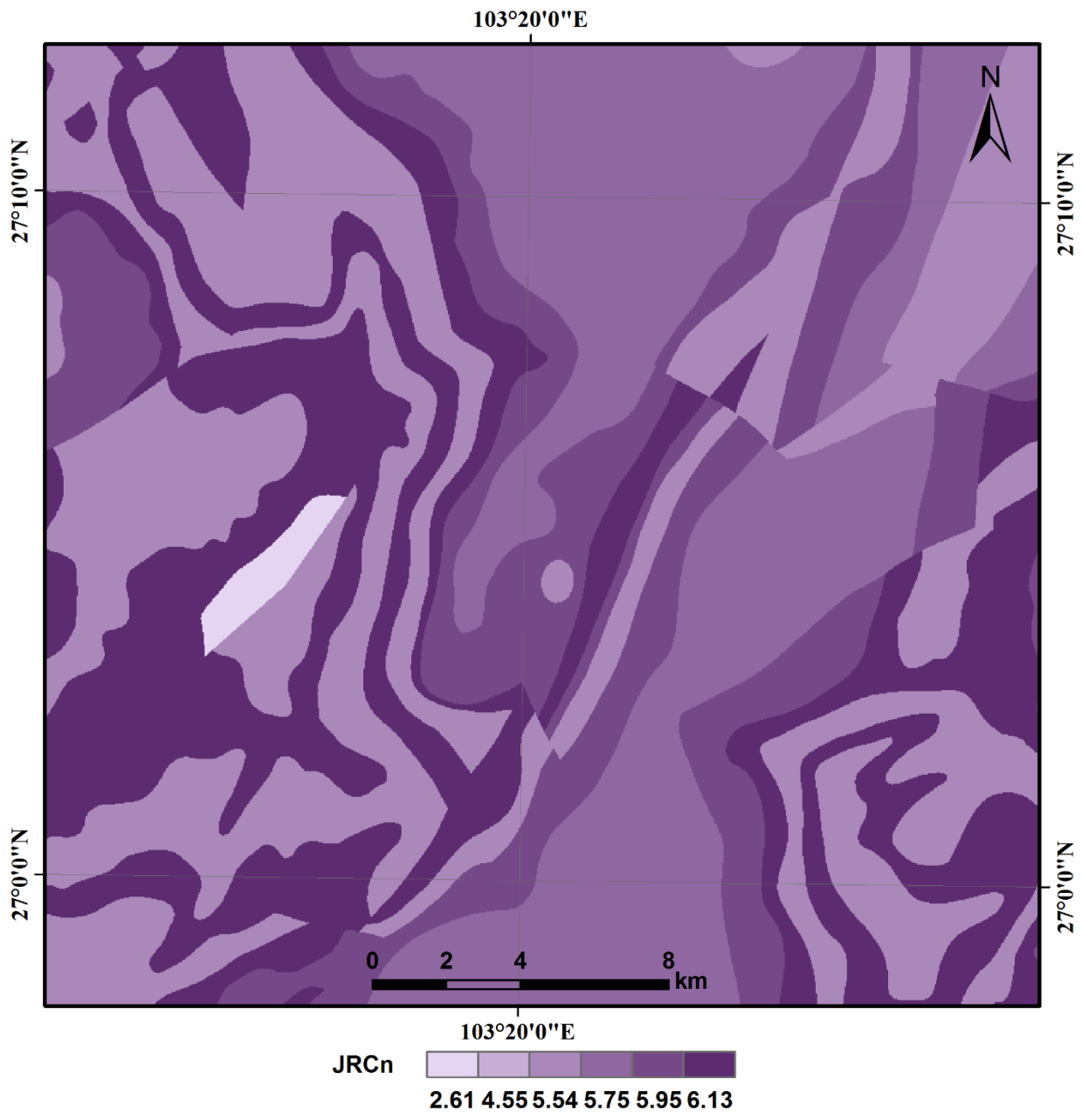
519

520 **Fig. 4.** Demonstration of the Newmark-analysis algorithm (adapted from [Wilson and Keefer, 1983](#); [Jibson](#)  
 521 [et al., 1998, 2000](#)): (a) Acceleration-time history with critical acceleration (horizontal dotted line) of 20%g  
 522 superimposed. (b) Velocity of block versus time. (c) Displacement of block versus time.

523



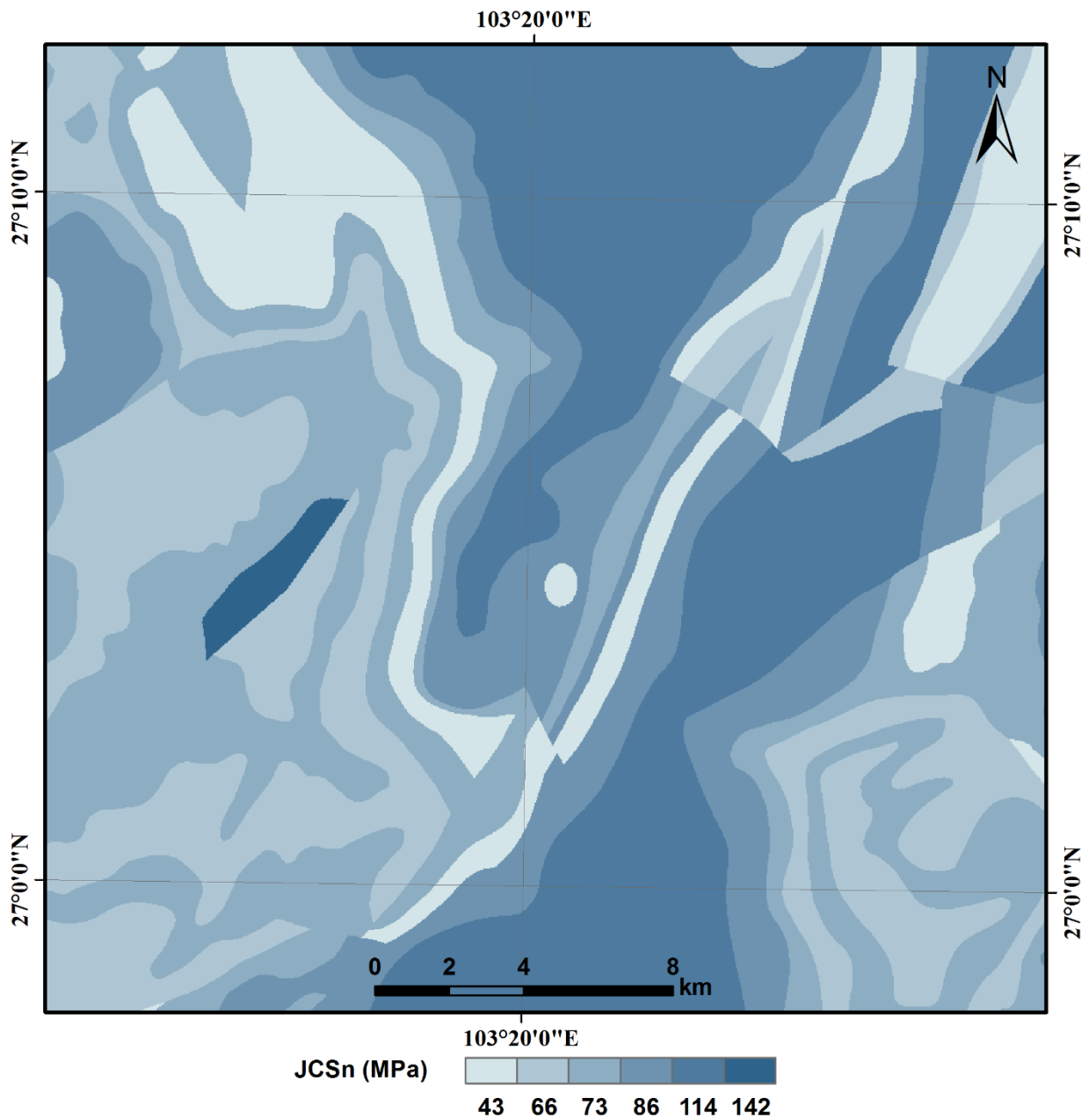
524  
525 **Fig. 5.** Slope map derived from the DEM of the study area.  
526



527

528

(a)



529

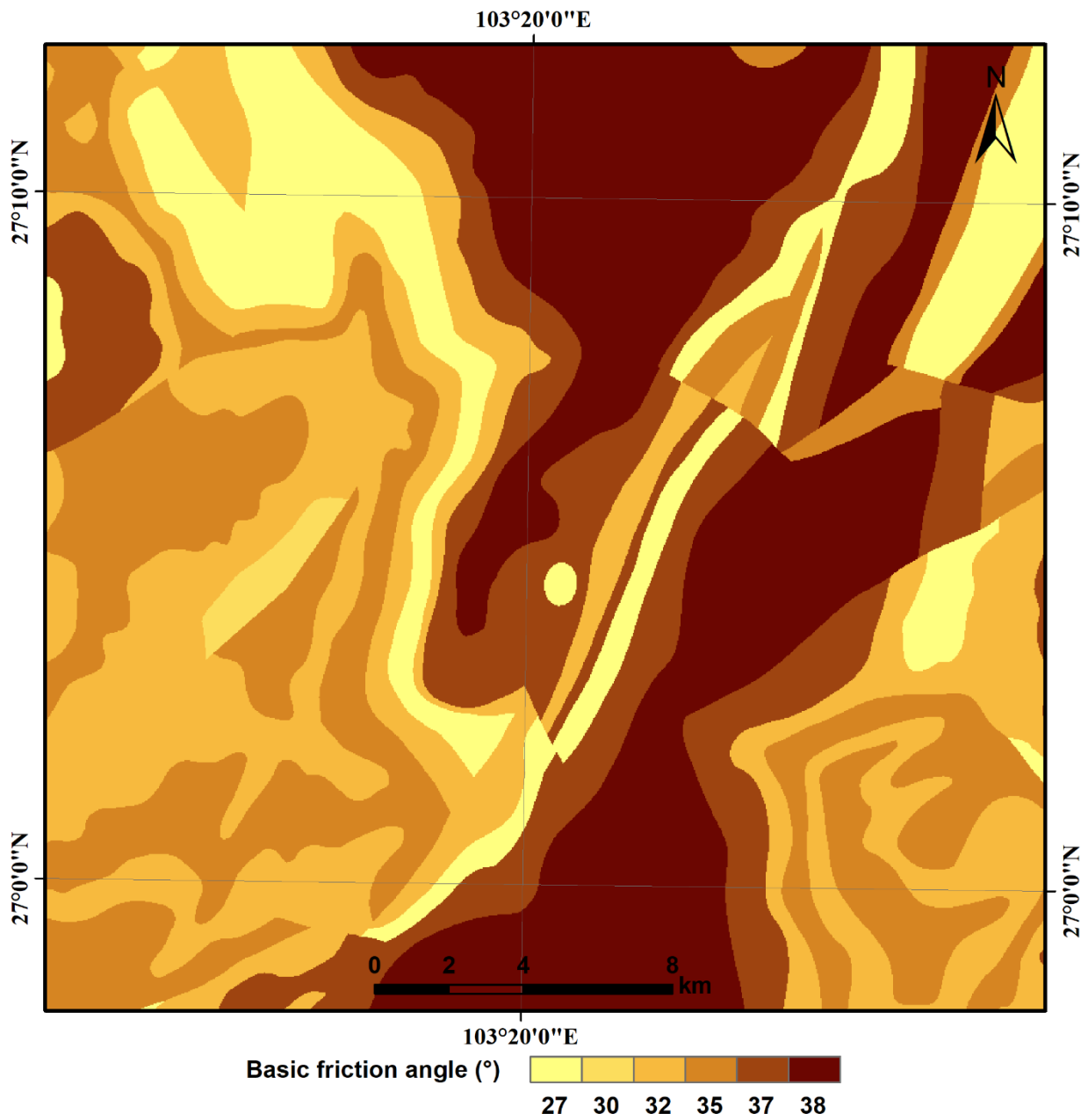
530

(b)

531 **Fig. 6.** (a)  $JRC_n$  component and (b)  $JCS_n$  component of shear strength assigned to rock types in the

532 study area.

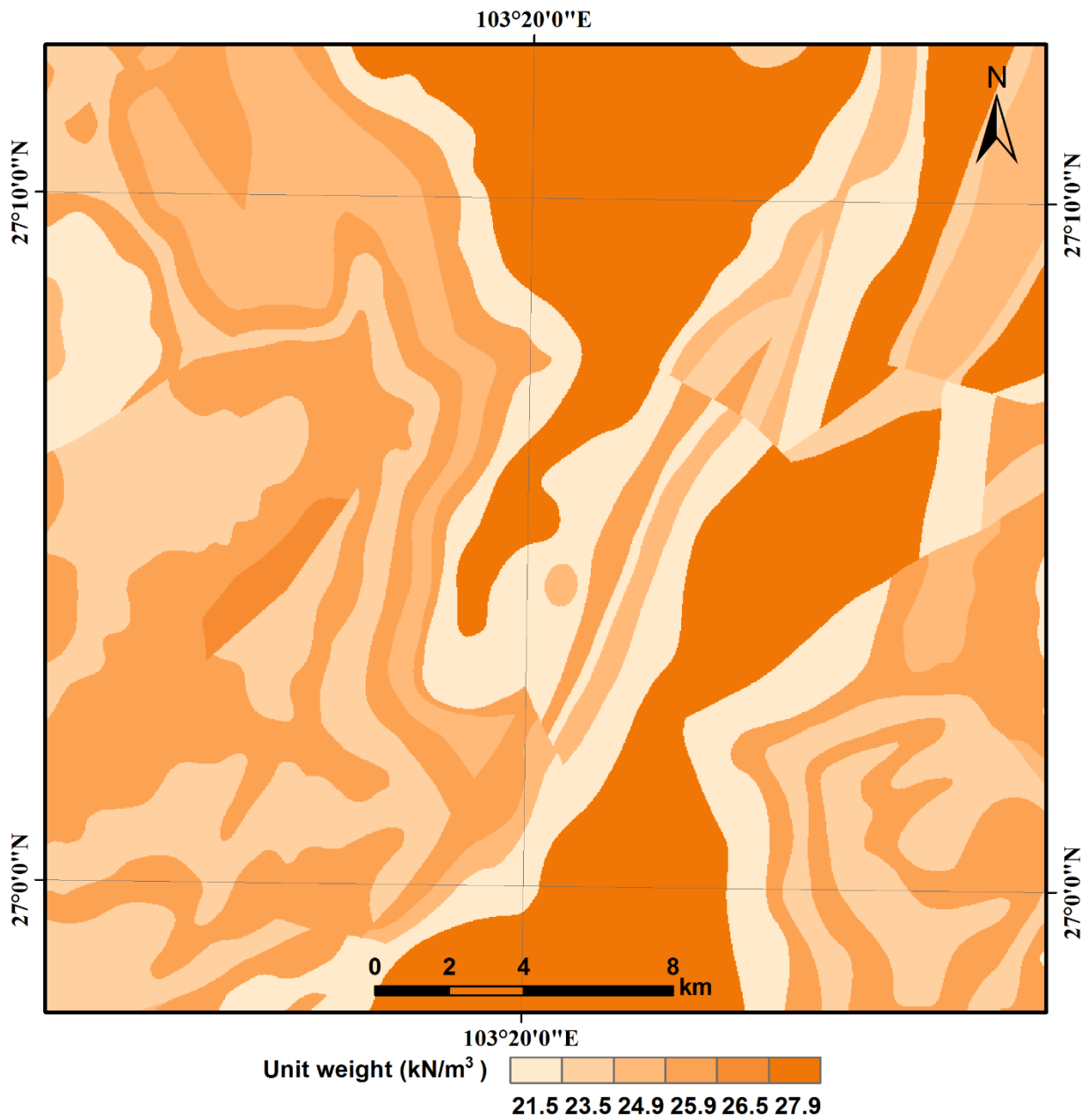




534

535 **Fig. 7.** Basic-friction-angle ( $\phi_b$ ) component of shear strength assigned to rock types in the study area.

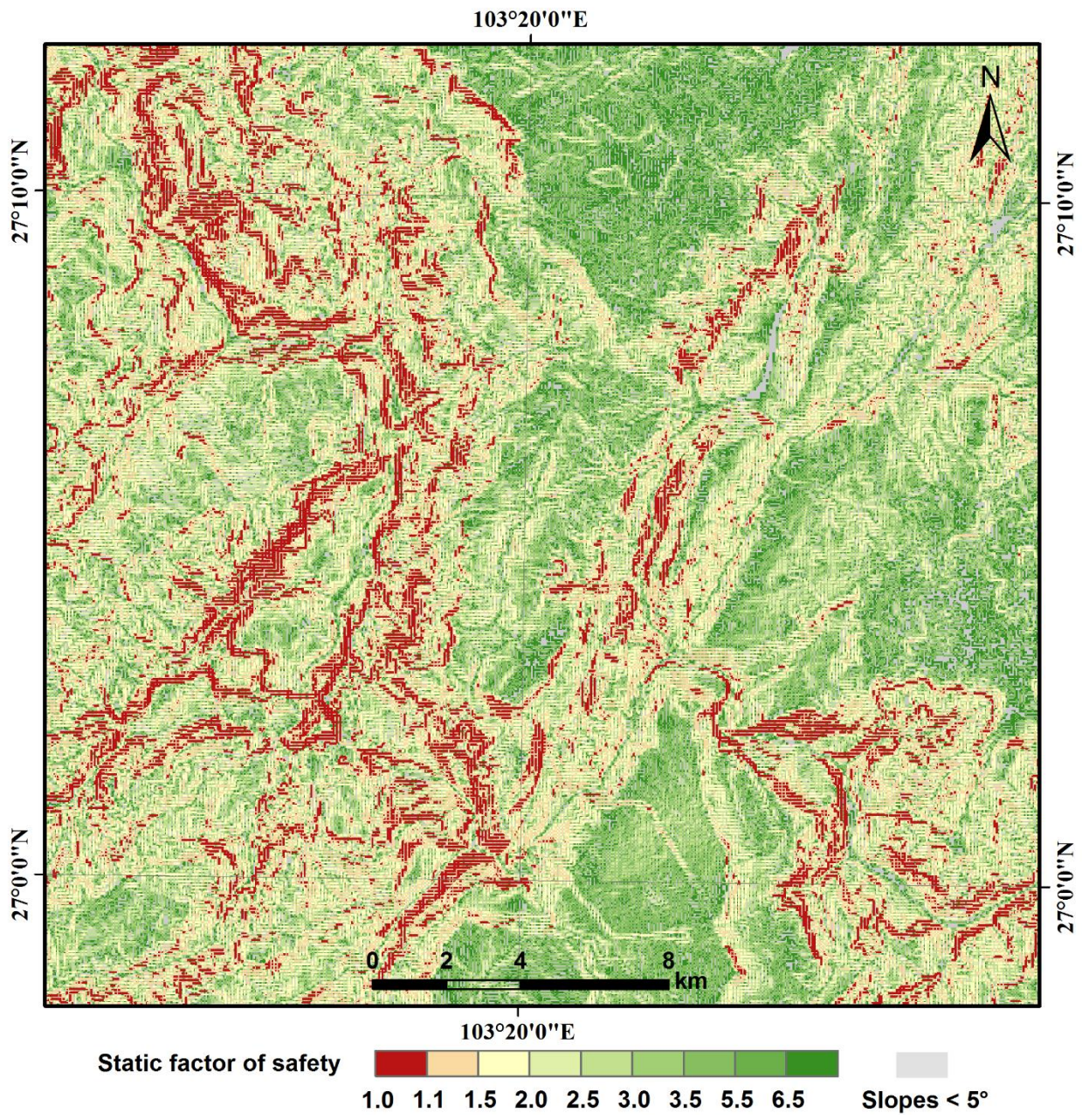
536



537

538 **Fig. 8.** Unit weight ( $\gamma$ ) assigned to rock types in the study area.

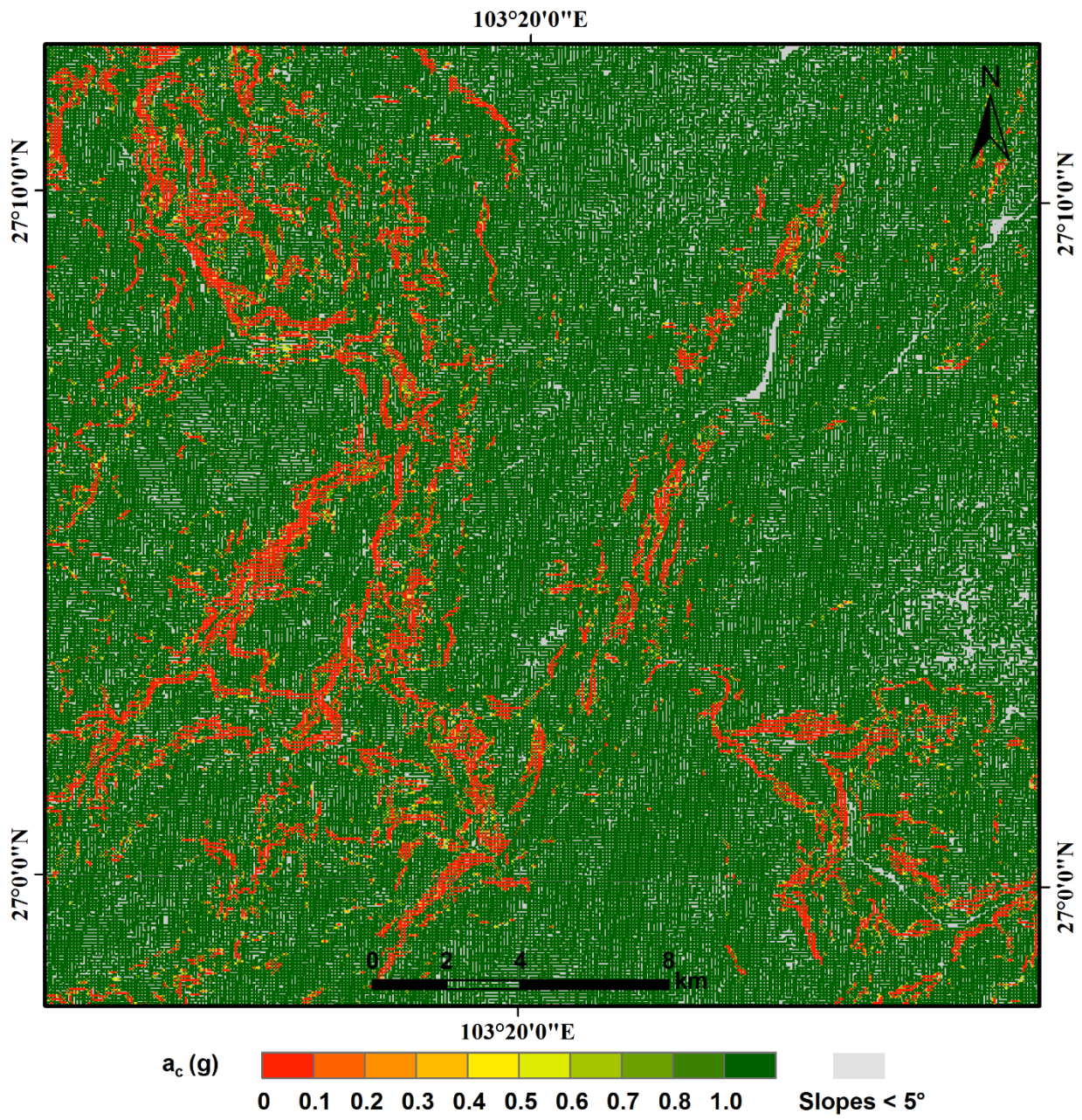
539



540

541 **Fig. 9.** Static factor-of-safety map of the study area.

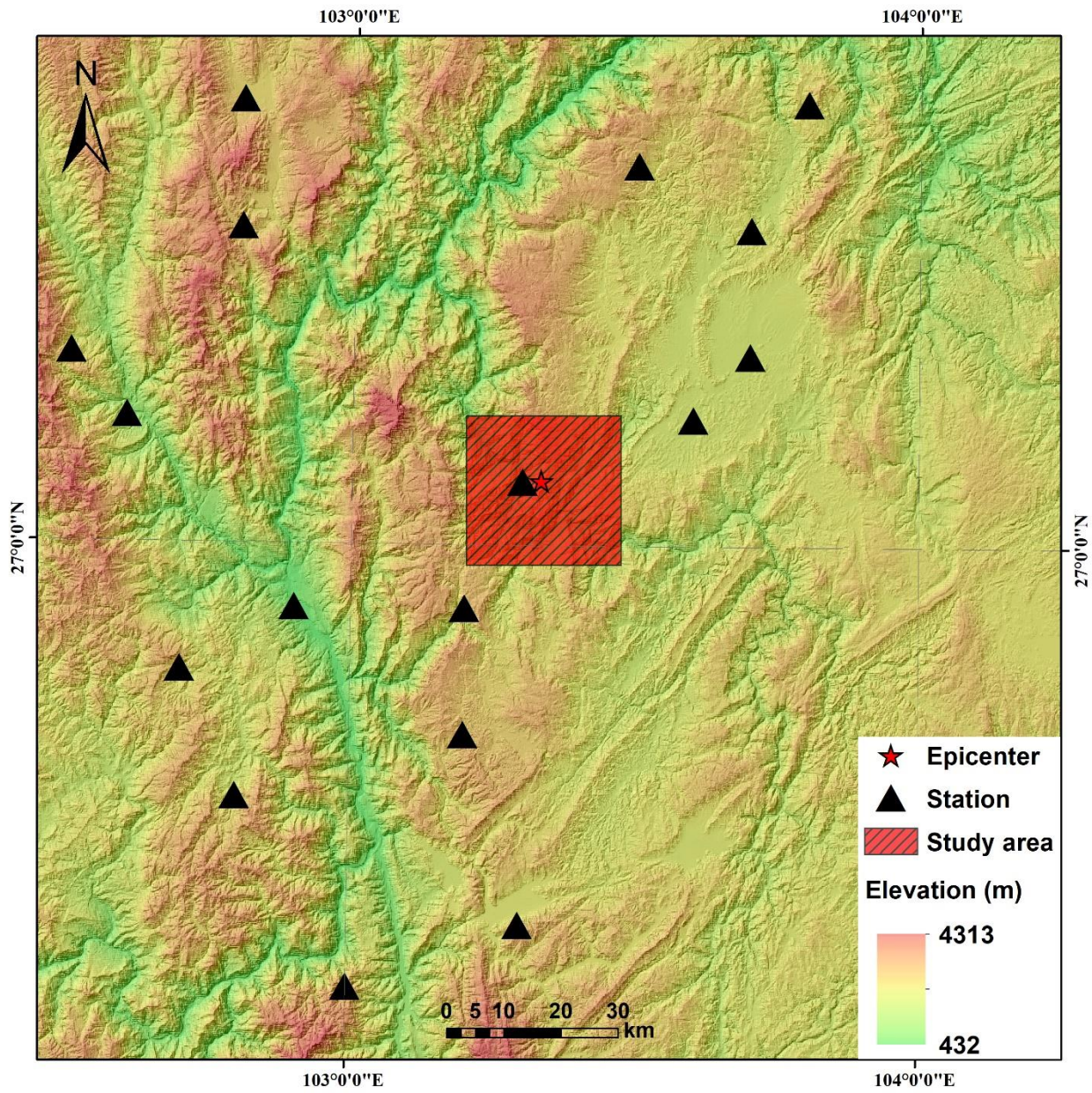
542

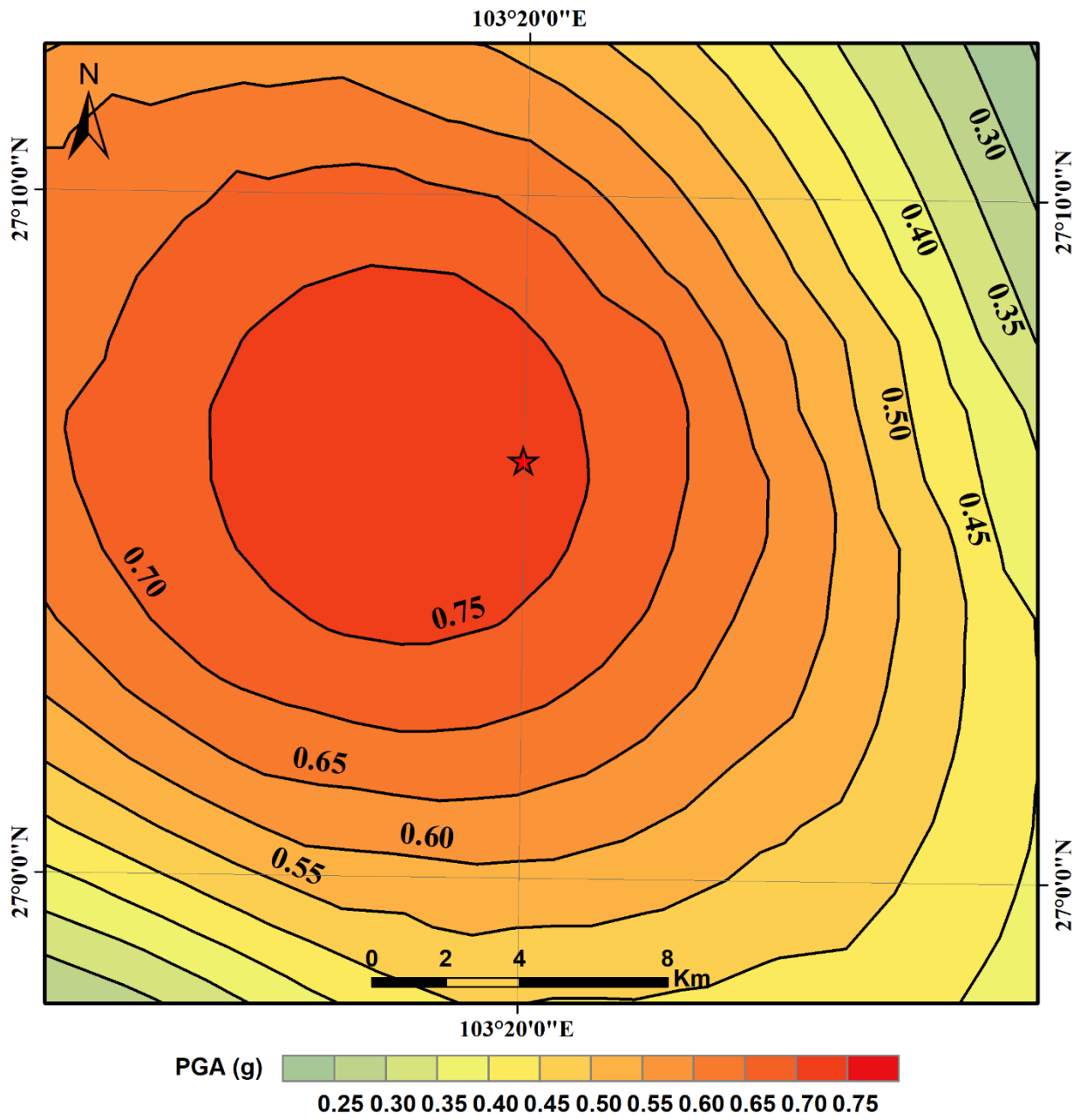


543

544 **Fig. 10.** Map showing critical accelerations in the study area.

545

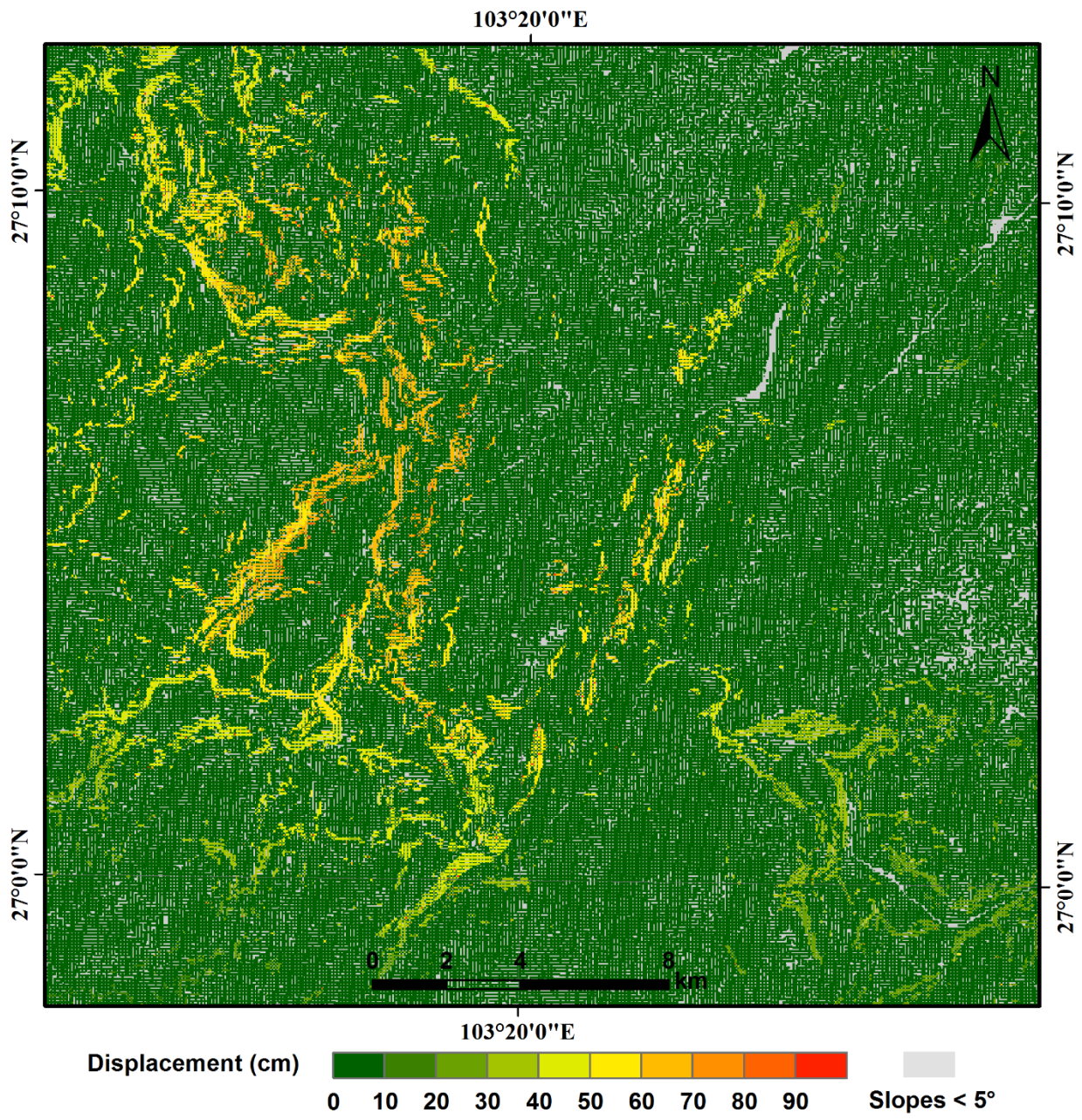




549

550 **Fig. 12.** Contour map of peak ground acceleration (*PGA*) produced by the Ludian earthquake in the  
 551 study area. *PGA* values shown are in *g*.

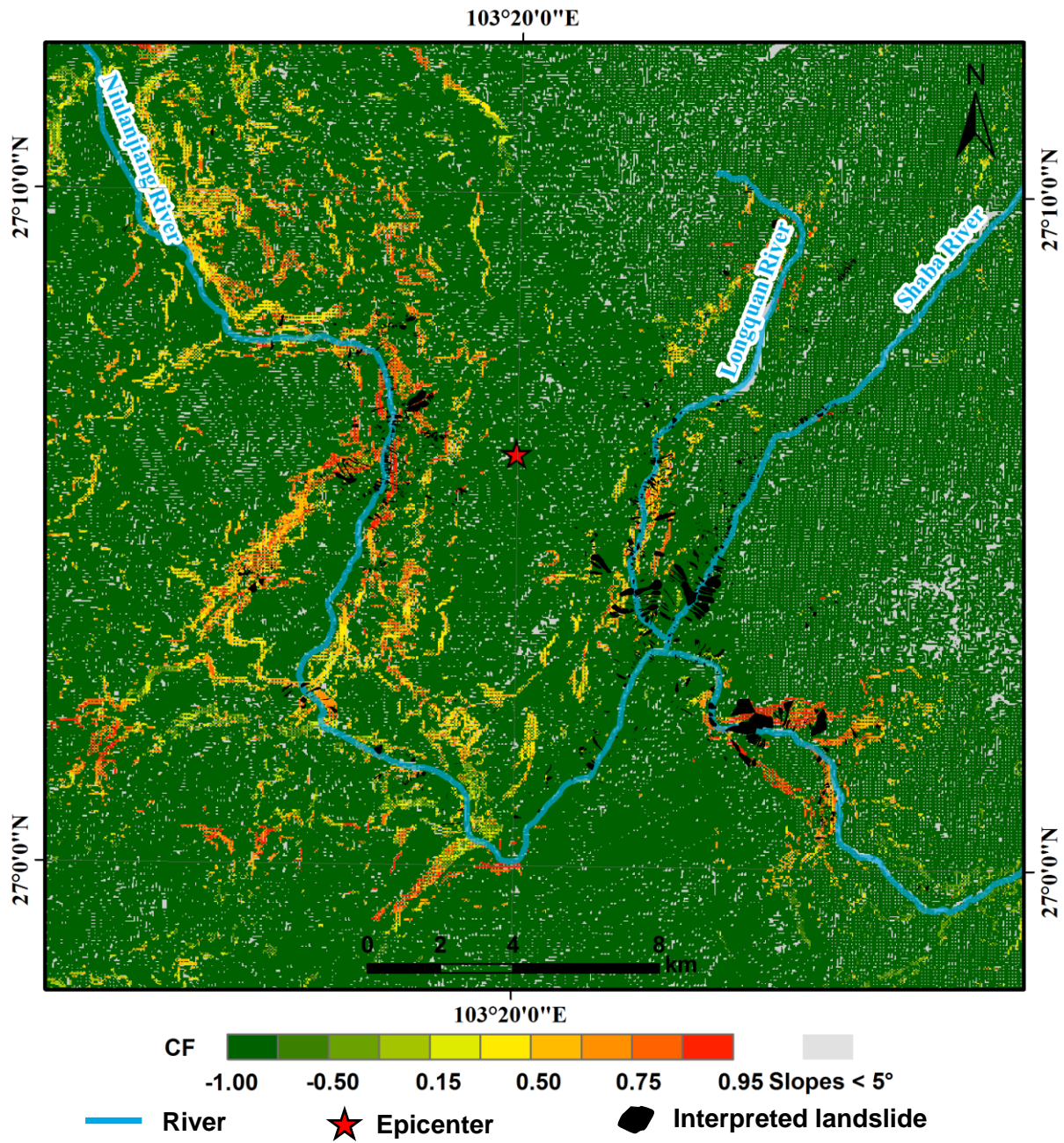
552



553

554 **Fig. 13.** Map showing predicted displacements in the study area.

555



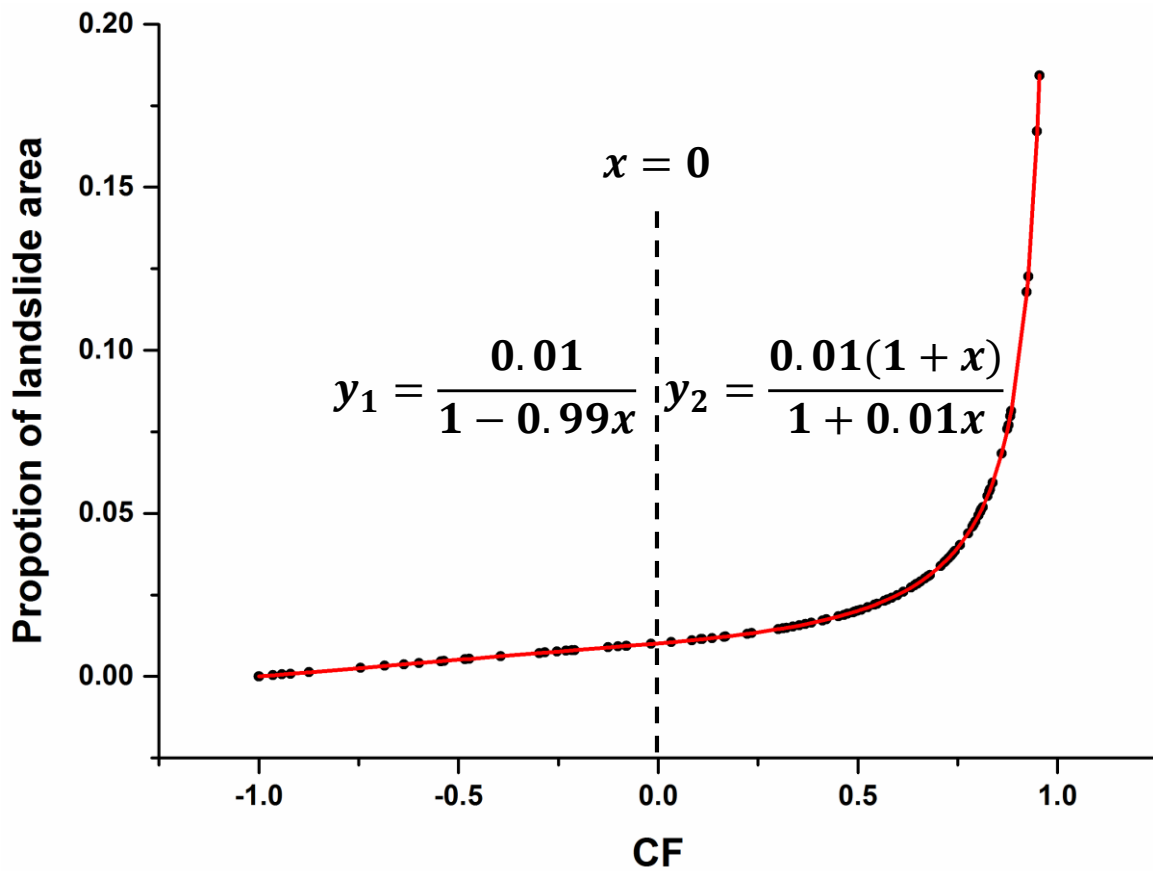
556

557 **Fig. 14.** Map showing confidence levels of coseismic landslides in the Ludian earthquake using method

558 introduced in this paper. Confidence levels are portrayed in terms of values of  $CF$ .

559

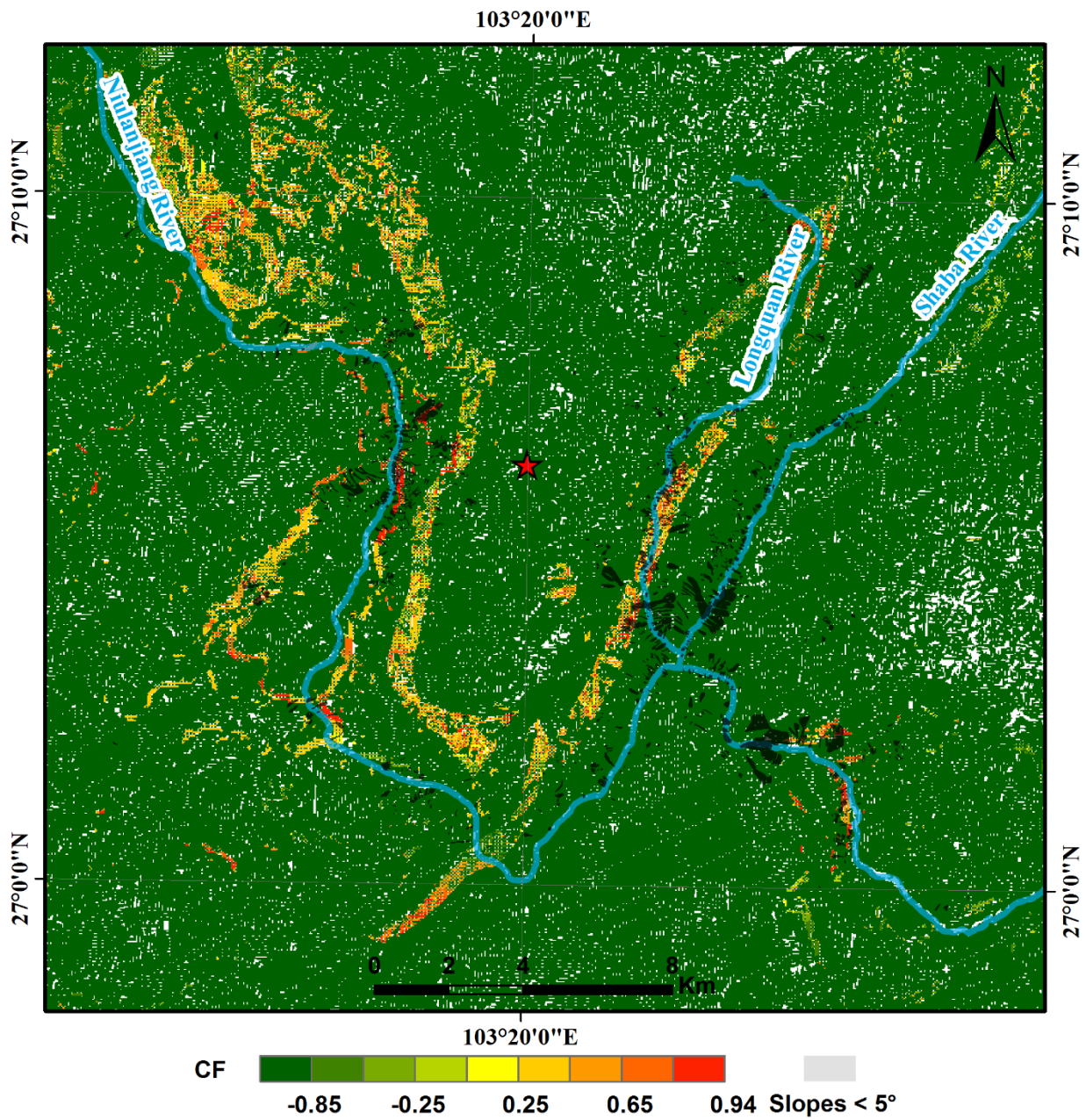
560



561

562 **Fig. 15.** Proportion of the area of landslides lying in each  $CF$ -value area. A dot shows the proportion of  
 563 landslide area within an area of  $CF$  value; the red line is the fitting curve of the data using second order  
 564 exponential growth function.

565



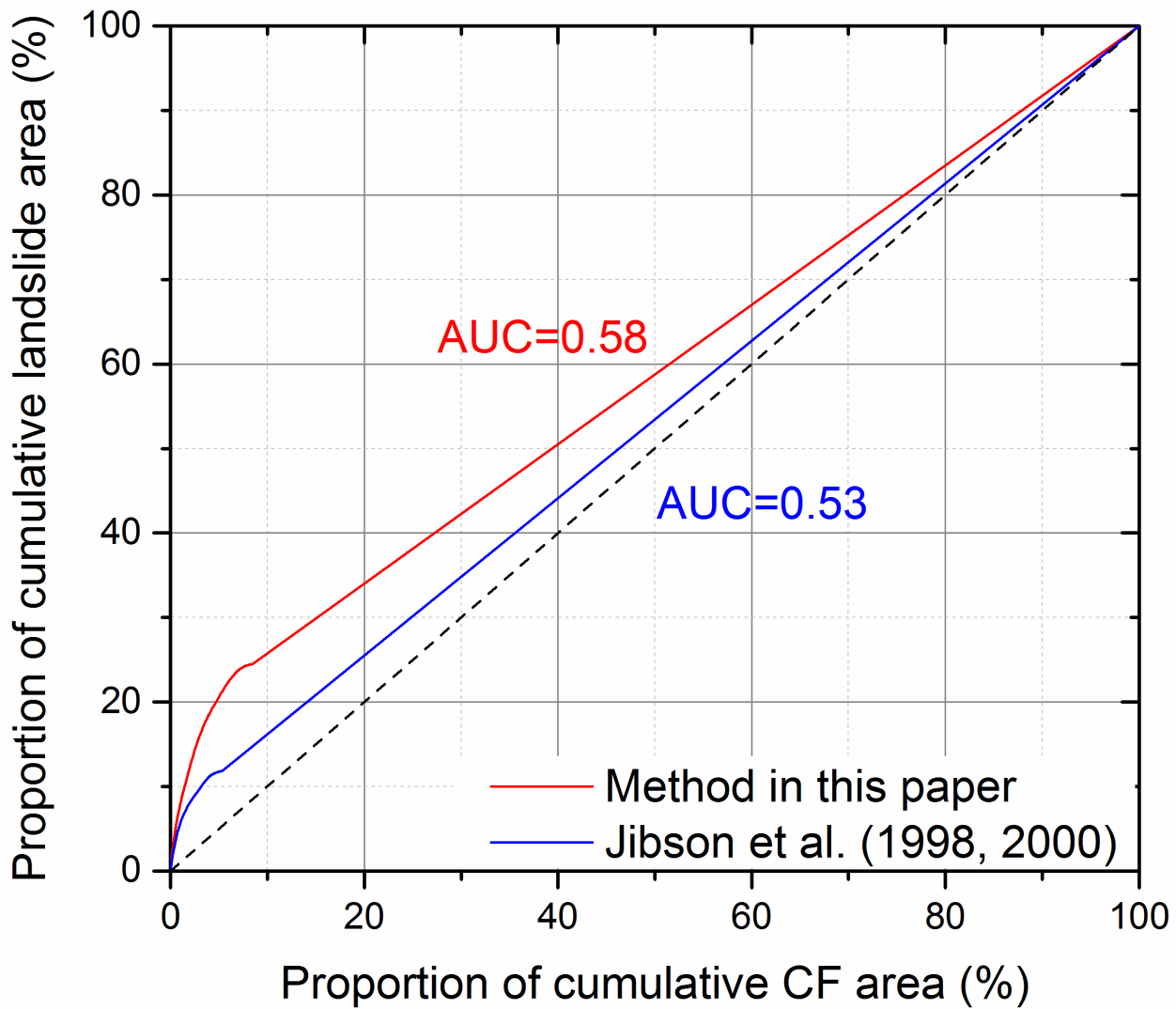
566

567 **Fig. 16.** Map showing confidence levels of coseismic landslides in the Ludian earthquake using a

568 conventional Newmark analysis. Confidence levels are portrayed in terms of values of *CF*.

569





571

572 **Fig. 17.** Area under the curve plots for comparing the new method with a conventional Newmark's

573 method.

574

575

576 **Table Captions**

577 **Table 1.** Shear strengths assigned to rock types in the study area.

578 **Table 2.** Station records included three components of the peak ground acceleration.

579

580

581 **Table 1**

582 Shear strengths assigned to rock types in the study area.

Rock type	$\gamma$ (kN/m <sup>3</sup> )	$\phi_b$	$JCS_0$ (MPa)	$JRC_0$	$\varphi$	$c$ (kPa)	References
Dolomite	25.9	32°	140	9.5	43°	35	<a href="#">Singh et al., 2012</a> <a href="#">Giusepone, 2014</a> <a href="#">Alejano et al., 2014</a> <a href="#">Bandis et al., 1983</a>
Limestone	21.5	37°	160	9	45°	30	<a href="#">Singh et al., 2012</a> <a href="#">Yong et al., 2018</a> <a href="#">Barton and Choubey, 1977</a>
Shale	24.9	27°	75	8	27°	16	<a href="#">Bilgin and Pasamehmetoglu, 1990</a> <a href="#">Coulson, 1972</a>
Sandstone	23.5	35°	100	6	42°	24	<a href="#">Bandis et al., 1983</a> <a href="#">Priest, 1993</a> <a href="#">Coulson, 1972</a>
Basalt	27.9	38°	205	8.5	50°	40	<a href="#">Barton and Choubey, 1977</a> <a href="#">Alejano et al., 2014</a> <a href="#">Coulson, 1972</a> <a href="#">Barton and Choubey, 1977</a>
Slate	26.5	30°	175	3	40°	11	<a href="#">Bandis et al., 1983</a> <a href="#">Alejano et al., 2012</a> <a href="#">Yong et al., 2018</a>

583 Internal friction angle ( $\varphi$ ), cohesion ( $c$ ) and unit weight ( $\gamma$ ) are derived from Geological Engineering  
 584 Handbook ([Geological Engineering Handbook Editorial Committee, 2018](#))

585

587 Station records included three components of the peak ground acceleration.

No.	Station	Epicentral distance (km)	EW (g)	NS (g)	UD (g)	Average of horizontal components (g)
1	Longtoushan 1	8.114	0.5141	0.9679	0.7193	0.7410
2	Longtoushan 2	8.3	0.9685	0.7203	0.5147	0.8444
3	Qianchang	18.6	0.1490	0.1432	0.0539	0.1461
4	Ciyuan	32.6	0.0468	0.0457	0.0265	0.0463
5	Mashu	38.5	0.1380	0.1361	0.0663	0.1370
6	Qiaojia	43	0.0253	0.0210	0.0135	0.0232
7	Zhaotong 1	47.4	0.0096	0.0152	0.0065	0.0124
8	Zhaotong 2	47.671	0.0065	0.0096	0.0088	0.0081
9	Huidongxijie	63.3	0.0123	0.0128	0.0037	0.0126
10	Maolin	64.4	0.0251	0.0184	0.0111	0.0217
11	Yongshanmaolin	65.647	0.0111	0.0252	0.0184	0.0182
12	Jingan	66.2	0.0103	0.0122	0.0062	0.0113
13	Butuotuoju	66.8	0.0118	0.0173	0.0079	0.0146
14	Zhaotongjingan	67.392	0.0062	0.0103	0.0122	0.0083
15	Huidongqianxin	67.4	0.0224	0.0223	0.0067	0.0224
16	Ningnansongxin	69.2	0.0062	0.0081	0.0032	0.0071
17	Pugebaishui	76	0.0152	0.0149	0.0066	0.0151
18	Huize	76.5	0.0164	0.0182	0.0090	0.0173
19	Pugediban	81.2	0.0186	0.0127	0.0046	0.0156
20	Butuodiban	83.7	0.0024	0.0021	0.0024	0.0023

21	Tuobuka	85.2	0.0168	0.0168	0.0136	0.0168
22	Pugeyangwo	91.4	0.0066	0.0069	0.0022	0.0068
23	Daguan	91.8	0.0043	0.0035	0.0027	0.0039

---

588

589